Podiform magnetite ore(s) in the Sabzevar ophiolite (NE Iran): oceanic hydrothermal alteration of a chromite deposit

Alireza Eslami, Benjamin Malvoisin, Fabrice Brunet, Ali Kananian, Wolfgang Bach, Giovanni Grieco, Alessandro Cavallo, G. Diego Diego Gatta

Podiform magnetite ore(s) in the Sabzevar ophiolite (NE Iran): Oceanic hydrothermal alteration of a chromite deposit

Alireza Eslami[1,2], Benjamin Malvoisin[2], Fabrice Brunet[2], Ali Kananian[1*], Wolfgang Bach[3], Giovanni Grieco[4], Alessandro Cavallo[5], G. Diego Gatta[4]

[1]School of Geology, College of Science, University of Tehran, Tehran 1417614418, Iran

[2]ISTerre, Univ. Grenoble Alpes, Univ. Savoie Mont Blanc, CNRS, IRD, IFSTTAR, 38041 Grenoble, France

E-mail address: kananian@ut.ac.ir

[3]Geoscience Department, University of Bremen, Klagenfurter Str., 28359 Bremen, Germany

[4]Dipartimento di Scienze della Terra, Università degli Studi di Milano, via S. Botticelli 23, I-20133 Milano, Italy

[5]Dipartimento di Scienze dell'ambiente e del territorio e di Scienze della terra, Università di Milano-Bicocca, I-20126 Milano, Italy

Abstract

Serpentinite-hosted massive magnetite ore bodies are reported for the first time in the Late Cretaceous Sabzevar ophiolitic belt, northeastern of Iran. They show irregular and discontinuous shapes with variable sizes ranging from 30 to 60 cm. Chromian spinel grains are observed within both magnetite ores and host serpentinite. Magmatic chromian spinels, (Cr,Al)-spinel I, with compositions close to $(Mg_{0.6},Fe_{0.4})(Cr_{1.2},Al_{0.75},Fe^{3+}_{0.05})O_4$ are preserved in the host serpentinite where they display a porous alteration rim composed of Cr-bearing chlorite and three different spinel-structure minerals: Cr-spinel $(Fe_{0.6},Mg_{0.4})(Cr_{1.4},Al_{0.4},Fe^{3+}_{0.2})O_4$, named Cr-spinel II (second generation), magnetite and ferritchromite, nominally $FeCr_2O_4$. In the magnetite ore body, no (Cr,Al)-spinel I is found and Cr-spinel II occurs as relict cores surrounded by ferritchromite and magnetite. Detailed X-ray elemental mapping revealed that the 200 μm-thick magnetite rim is composed of two magnetite types with different minor element compositions: the first rim found at the contact with ferritchromite is thin (20 μm; magnetite-I); the thicker outer rim contains numerous Fe-poor and Mg- and Si-rich silicate inclusions (magnetite-II). Observations at the TEM scale allows to identify ferritchromite which occurs as a micrometer-sized rim between Cr-spinel II and magnetite I. Thermodynamic modelling of the phase relationships in the studied Sabzevar serpentinite suggests that Cr-spinel II is produced along with chlorite during a first alteration stage at temperatures between 725 and 575 °C in the course of peridotite-water interactions.

A second hydrothermal alteration stage producing ferritchromite and magnetite is inferred from the thermochemical modelling at temperatures < 400 °C under high H_2 fugacity. This latter stage corresponds to the serpentinization of the Sabzevar oceanic peridotite and associated podiform chromitite deposit. The two alteration stages are interpreted as the result of the interaction between seawater and oceanic mantle at two different depth ranges in the course of its exhumation. Our thermodynamic calculations and textural relationships revealed that Cr is immobile and Fe is the main element to be transferred to the magnetite ore during alteration processes. Fe possibly originated from direct transport of the Fe^{2+} produced during olivine dissolution or from the dissolution of nano-sized magnetite grains initially formed in the host serpentinite during early serpentinization. Mass balance calculation reveals significant iron transport at a scale > 10 m during serpentinization.

Keywords: Serpentinization; epitaxial growth; ferritchromite; iron segregation; ASTAR

1. Introduction

Magnetite ore bodies hosted by serpentinites have been described in several ophiolites worldwide, in Morocco (Bou-Azzer, e.g. Gahlan et al., 2006; Gahlan and Arai, 2007), in Greece (Olympus, Vermion, Edessa and Skyros Island; Paraskevopoulos and Economou, 1980), in central Iran (Nain; Eslami et al., 2018a), in the Bangong–Nujiang suture zone in Tibetan Plateau (Angwu, Cebojiyi, Beila, and Daru Co; Liu et al., 2019), in Southern Oman (Aniba; Khedr and Arai, 2018) and in the Western Alps (Southern Aosta Valley; Rossetti et al., 2009; Carbonin et al., 2015; Della Guista et al. 2011; Toffolo et al., 2017) among others. In all these occurrences, magnetite ores form massive, nodular and banded ores with an overall thickness that can vary from a few centimeters up to 50 m and with lengths typically between 2 and > 500 m. The processes involved in such a large iron segregation, and their driving forces remain poorly understood and the characterization at various scales of serpentinite-hosted magnetite ores is therefore needed.

Magnetite ore formation can also be associated with magmatic spinel alteration. Spinel composition is often used to determine the melting degree in residual peridotites (Dick and Bullen, 1984), along with mantle oxygen fugacity (O'Neil and Wall, 1987). The application of these two widely used proxies requires deciphering the modification of the original spinel composition by late magmatic processes, hydrothermal alteration and/or metamorphism.

It is well established that the hydrothermal alteration of peridotites at temperatures below 400 °C (i.e. serpentinization) induces the oxidation of the iron initially contained in olivine and pyroxene, leading to magnetite formation (e.g., Moody, 1976; Oufi et al., 2002). Magnetite is often found as disseminated grains in the serpentinite matrix or concentrated in mesh textures and in veins implying a

certain extent of remobilization (Beard et al., 2009). A first possible view is that the formation of large ore bodies during serpentinization (or during a later metamorphic stage), implies iron mobilization at a large scale (e.g. Gahlan et al., 2006; Eslami et al., 2018a). Olivine and pyroxene serpentinization could then be the source of that iron (Prabhakar and Bhattacharya, 2013). The respective role of water/rock ratio, temperature, oxygen fugacity and chemical potential gradients in driving this wide iron segregation still needs to be clarified.

In serpentinite-hosted magnetite ores, magmatic chromium spinels, $(Mg,Fe)(Al,Cr,Fe)_2O_4$, may also play a key role in magnetite formation (e.g. Kimball, 1990; Colas et al., 2019), as they are commonly found in the core of the magnetite grains (Michailidis, 1990; Barnes, 2000; Barra et al., 2014). However, the link between magnetite formation and Cr-spinel alteration is strongly debated.

Thermodynamic modelling predicts the formation of magnetite and ferritchromite ($FeCr_2O_4$) at the expense of Cr-spinel at temperatures below ~ 550°C (Sack and Ghiorso, 1991). Hence, the iron involved in magnetite formation at the Cr-spinel surface could be derived locally from Cr-spinel dissolution (Ulmer, 1974). The formation of magnetite and ferritchromite at the expense of Cr-spinel requires reactions in an open chemical system with Al and Cr removal or dilution. These two elements are often considered as largely immobile in geochemical processes. The solubility, and thus the mobility, of Cr depends on its oxidation state and on the presence of ligands, such as chlorine, which can complex chromium and enhance its solubility (Huang et al., 2019). Divalent and hexavalent chromium are actually orders of magnitude more soluble than trivalent chromium, Cr(III). The same type of solubility contrasts holds also true for Fe (II) and Fe(III), and therefore redox potential (or oxygen fugacity) has been logically identified as a key parameter in the formation of serpentinite-hosted magnetite ores. Indeed, redox conditions may vary considerably depending on whether the magnetite ore formed during serpentinization, which would produce H_2 (Kimball, 1990), or during late stage fluid-rock interactions under more oxidizing conditions (Gervilla et al., 2012; Barra et al., 2014).

Here, for the first time, we report a distinct suite of m-scale pod-like bodies of massive-textured magnetite with a cataclastic fabric from the Late Cretaceous Sabzevar ophiolite in NE Iran. These magnetite ore bodies share striking resemblances to podiform chromitite deposits reported throughout the Sabzevar ophiolite belt by virtue of their common geological setting, analogous morphology and macroscopic characteristics. Serpentinized dunite encompasses the podiform magnetite and chromitite in the form of envelopes of variable thickness ($\geq$ 0.5 m). Chromium-rich spinel is occasionally found as relict core of magnetite grains inside the magnetite ore suggesting that the magnetite ores represent the transformation products of pre-existing semi-massive or weakly disseminated chromitite. Spinel in both magnetite ore and host serpentinite shows an intricacy of mineralogical, structural and geochemical fingerprints resulting from a multi-stage alteration history.

We present here a detailed mineralogical description of the new magnetite ore occurrence with a particular emphasis on the micro-nanotextural relationship between chromite and magnetite in both magnetite ore and host serpentinite. Both phase relationships in the host serpentinite and fluid

compositions were modeled in order to interpret the micro- and nanoscale observation. A conceptual model for the genesis of magnetite ore in the Sabzevar ophiolite is eventually proposed that involves significant iron mass transfer from the serpentinite to the magnetite ore.

2. Geological setting and magnetite-ore occurrence

Several podiform chromitite ores have been described in the western and central part of the Sabzevar ophiolite (Shafaii Moghadam et al., 2013, 2015). Here we describe a first occurrence of podiform magnetite ores in the eastern sector (N36°32'55", E57°00'00") of the northern Sabzevar ophiolite belt (called Sabzevar ophiolite). Sabzevar ophiolite shows a general SE-NW trend and it forms a continuous belt, about 150 km long, consisting of thrust-bounded blocks of Neotethyan oceanic lithosphere (Fig. 1b). The Sabzevar ophiolitic belt is often interpreted as having formed in an arc-related oceanic basin (e.g., Noghreyan, 1982; Jafari et al., 2013; Shafaii Moghadam et al., 2015; Omrani, 2018; Rahmani et al., 2020). More specifically, Sabzevar ophiolites are believed to represent an embryonic, subduction-related oceanic basin that opened between the Lut Block to the South and Turan block to the North since at least mid-Cretaceous time (Shafaii Moghadam et al., 2014).

The eastern sector of the Sabzevar ophiolite is dominantly composed of a km-scale peridotite massif, which is locally crosscut by rodingitized microgabroic-diabasic dykes, by gabbroic intrusions and by Middle Eocene dacitic domes (Fig. 1c). Seafloor alteration and low-grade metamorphism have been recorded in basaltic sequence of the Sabzevar ophiolite (Shojaat et al., 2003). Such modification can be tracked in diabase and metasomatized (spilitic) pillow lavas in the studied area. Although occurrences of retrogressed mafic granulitic bodies embedded in ophiolitic nappes have been reported from the northern parts of the Sabzevar ophiolite (Rossetti et al., 2010), there is no indication of high pressure metamorphism in the study area. We observed several massive and rarely disseminated pod-like chromitite bodies ranging from a few centimeters to a few tens of meters in diameter. They are hosted in dismembered masses of harzburgite in a brittle shear zone. Irregular and discontinuous trails of podiform magnetite-ore bodies occurred within highly sheared serpentinite masses (Fig. 2a). These ores occur as a series of boudins and elongated lenses that can be tracked over a distance of a few tens of meters along a roadcut.. The contacts between the magnetite ores and the host serpentinite are usually sharp (Fig. 2b). Small aggregated masses of octahedral magnetite crystals with variable sizes are barely visible to the naked eye on hand specimen (Fig. 2c).

3. Methods

3.1 Bulk sample characterization

In total, nine specimens from individual magnetite pods and six samples from the host serpentinites were collected in the studied area (Fig. 2). Polished thin-sections of the corresponding samples were examined under transmitted and reflected light using a Leica optical microscope.

All collected rock samples were also crushed using a hydraulic press down to a grain size ≤ 2 mm. Subsequently, the granular material was milled with an agate ball mill for 15 minutes at 500 revolutions per minute. The obtained powders from each sample were mixed and quartered for the preliminary measurement of LOI (loss on ignition).

Major element concentrations and loss-on-ignition (LOI) of the host peridotite bulk samples (MG21, MG20 and MG16) were determined at the University of Milan Bicocca. Major element concentrations were measured by energy-dispersive X-ray fluorescence (EDXRF) on fused glass disks with a PANalytical Epsilon 3-XL spectrometer. The collected data were preliminary analyzed with the Malvern Panalytical Epsilon 3 software platform, using the Omnian - standardless model, which allows qualitative and quantitative chemical analysis of unknown materials without the construction of calibration lines. The quantitative analysis was then repeated in 6 different instrumental conditions, using the Panalytical WROXI® – synthetic, high quality Certified Reference Materials for calibration.

3.2 Micro- and nano-scale characterization

Quantitative chemical analyses of individual spinel and silicate minerals were collected using a JEOL JXA-8230 electron probe micro-analyzer (EPMA) equipped with five wavelength-dispersive spectrometers (WDS) and an energy-dispersive spectrometer (EDS) at the Institut des Sciences de la Terre, University Grenoble Alpes, France. Analyses were performed at 15 kV acceleration voltage, 100 nA beam current and a beam size with a diameter of ~1 μm. The concentrations of minor and trace elements (Si, V, Ti, Ni, Co, Mn and Zn) and major elements (Fe, Cr, Al and Mg) were measured by WDS and EDS, respectively. Total counting times (peak plus background) were 440 s for Si Kα; 240 s for V Kα, Ti Kα; 360 s for Co Kα; 180 s for Zn Kα; 100 s for Ni Kα and Mn Kα. Natural minerals, pure metals and synthetic oxides were used as standards and the ZAF correction was applied. Spectral interference (V Kα vs Ti Kβ) was corrected using the JEOL software-calculated correction factor. The detection limits varied between 0.005 and 0.02 wt%, using 3-sigma criterion (Batanova and al., 2018). Elemental distribution maps were collected using an accelerating voltage of 15 kV, a beam current of 200 nA and a dwell time of 700 ms.

Sulfide phases were analyzed using a four-WDS spectrometer CAMECA SX100 electron microprobe analyzer (EMPA) at Department of Geosciences, University of Bremen, Germany. Accelerating voltages of 20 kV and beam current of 20 nA were used. Peak counting times varied between 20 and 40 s per element. The reference materials included synthetic compounds (i.e., Co, ZnS,

and FeS_2) as well as mineral standards (As: arsenopyrite, Mn: ilmenite, Fe: pyrite, Co: native cobalt, Ni: native nickel, Cu: chalcopyrite, Zn: sphalerite, S: pyrite, Pb: galena, Sb: antimonite).

Chromite/magnetite contacts were characterized at the nanoscale in the magnetite ore by Transmission Electron Microscopy (TEM). A TEM lamella was first extracted from a petrographic thin section across a reaction zone surrounding chromite (sample MG15, location on Fig. 5) and thinned to < 100 nm with a Ga+ focused ion beam using a Zeiss™NVision 40 Crossbeam at the Interdisciplinary Center for Electron Microscopy (CIMe$^-$-EPFL, Lausanne, Switzerland). After attaching the TEM foil to a copper grid, we acquired high-angle annular dark-field images (HAADF) and high-resolution images (HRTEM) with a Tecnai™Osiris microscope operated at 200 keV (CIMe$^-$ - EPFL, Lausanne). The composition at the chromite/magnetite interfaces was determined by combining Scanning Transmission Electron Imaging (STEM) with Energy Dispersive Spectrometry (EDS) mapping using a Field Electron Gun JEOL™ 2100F TEM operated at 200 keV (CMTC, Grenoble, France). The maps were corrected for thickness variation by scaling the number of counts with the oxygen map. This latter instrument was also used in combination with an automatic crystallographic orientation tool (ASTAR™; Rauch and Véron, 2014) to acquire crystal orientation maps at the nanoscale. A 1.5 nm-wide electron beam was scanned over the region of interest while acquiring diffraction patterns with a spacing of 4 nm on a 500 x 500 grid. The collected diffraction patterns were compared to pre-calculated templates generated for chromite and magnetite. The best-matching template was used for indexation at each pixel in order to determine crystallographic orientation. The crystallographic data of Santos et al. (2005) were used for generating the chromite templates. The magnetite templates were generated from a mineral structure determined on a magnetite collected in the magnetite ore with X-ray diffraction data collected with an Oxford™ Diffraction Xcalibur-1 diffractometer at the University of Milan.

Serpentine minerals were characterized using a Horiba Jobin Yvon LabRAM HR Evolution micro-Raman spectrometer at the University of Milan Bicocca. Spectra were collected using a green Nd 532-nm laser source at a maximum output power of 300 mW. For each thin section, serpentine mineral determination relied on the analysis of about hundred different serpentine areas.

3.3 Thermodynamic modelling

Temperature - fO_2 stability diagrams were calculated with Perple_X (version 6.9.0; Connolly, 2005) to investigate the influence of temperature and oxygen fugacity on Cr-spinel stability at 500 MPa. The calculation was performed using the mean composition of the serpentinites collected in Sabzevar (average on samples MG21, MG20 and MG16; Si 34.39 mol.%, Al 0.56 mol.%, Cr 0.26 mol.%, Fe 4.25 mol.%, Mg 60.45 mol.%, Ca 0.10 mol.%), and a water to rock ratio of ~ 1. The use of such compositions to compute pseudosections implicitly requires to assume thermodynamic equilibrium at the centimeter scale. Evans et al. (2013) have shown that the scale of equilibrium is probably smaller during metasomatic events. The calculations performed here have thus to be seen as predictions of the state

towards which the rock should tend. The differences between the calculations and the observations will serve for discussing element mobility during reaction. We used the thermodynamic database for solid phases of Holland and Powell (2011) combined with the database of Sverjensky et al. (2014) for aqueous species (DEW19HP622ver_elements.dat file). This database includes the dataset for chromium aqueous species from Huang et al. (2019). It was extended by including the Fe-chromite and Mg-chromite endmembers from Klemme et al. (2009). The fluid speciation was evaluated during the optimization with lagged forward-calculations (Galvez et al., 2015). The mineral solid solutions considered were olivine (O(HP); Holland and Powell, 1996, 1998), clinopyroxene (Cpx(HP); Holland and Powell, 1996, 1998), chlorite (Chl(HP); Holland and Powell, 1996, 1998), antigorite (Atg(PN); Padrón-Navarta et al., 2013), brucite (B) and garnet (Grt(JH); Jennings and Holland, 2015). An additional solid solution was built for Cr-bearing spinel by using a reciprocal model and the parameters for non-linearity in Gibbs energy from Sack and Ghiorso (1991). This solid solution predicts a critical temperature of ~ 550°C for the Fe_3O_4-$FeCr_2O_4$ solvus, which is consistent with the Sack and Ghiorso (1991)'s solid-solution model (Fig. S1). The fluid was modelled with the generic molecular fluid equation of state of Perple_X considering H_2O and H_2 as possible solvents. The thermodynamic database and solid solution model files used in this study are provided in the Supplementary Materials.

The determination of the spinel composition evolution during cooling requires to estimate the fO_2. All oxygen fugacities are given relative to the fayalite-magnetite-quartz buffer (FMQ) as $\Delta\log_{10}f_{O2}$. Frost (1985) proposed to calculate an internal fO_2 buffer for ultramafic rocks by fixing the activities in Fe in the Fe-bearing phases (e.g. olivine, orthopyroxene and spinel). We used the same approach here but, as the calculation is performed for a fixed bulk rock composition, determining the fO_2 only requires one additional constraint on the composition. In the stability field of olivine (430 to 800°C), the fO_2 is determined by using the Mg/(Mg+Fe) ratio of olivine as the additional compositional constraint. This directly fixes the fO_2 in the divariant fields. In the trivariant fields, two fO_2 are calculated for a single Mg/(Mg+Fe) ratio in olivine, one at $\Delta\log_{10}f_{O2} > -3$ and the other at $\Delta\log_{10}f_{O2} < -5$. We selected the highest value of fO_2 which is continuous with the values determined in the divariant fields, and provides values consistent with the estimates of Frost (1985). The Mg/(Mg+Fe) ratio measured in olivine relicts found in the Sabzevar serpentinized dunite is ~ 0.92. This value is systematically higher than the range of ratios computed with the bulk rock composition of the Sabzevar serpentinite. To determine a bulk rock composition consistent with the Mg/(Mg+Fe) ratio measured in olivine, we performed several simulations with Fe contents higher than in the Sabzevar serpentinite. We selected the composition for which 1) the value of 0.92 is encompassed in the calculated Mg/(Mg+Fe) ratio in olivine, and 2) the spinel composition at 800°C is consistent with typical spinel composition from ophiolitic forearc peridotite ($Cr^{3+} \sim Al^{3+}$; $Fe^{3+} < Cr^{3+}/Al^{3+}$). The iron concentration in the selected bulk rock composition is by20% higher than that of the analyzed Sabzevar serpentinite samples. This selected composition is further used to determine the variation of fO_2 with temperature along the isopleth of Fo_{92} olivine composition. At low temperature, where olivine is not stable, the additional compositional constraint

used to fix the fO_2 is the amount of oxygen in the system. It was considered to be equivalent to the amount of oxygen in an assemblage composed of pure water and a ferrous peridotite (FeO only in the bulk rock composition). Such an assemblage is expected to represent a mantle rock undergoing serpentinization. The fO_2 determined with the two methods detailed above is displayed in Figures 11 and 13. It falls in the same range as the fO_2 estimated by Frost (1985) in a cooling peridotite.

4. Mineralogical and textural characteristics

4.1 Host serpentinite

The host serpentinite displays a typical mesh texture, with olivine kernels of around 80 μm in dimension, surrounded by serpentine and brucite. The scarcity of bastite suggests that the host protolith was a dunite. Magnetite is rare and occurs as euhedral grains with sizes up to 150 μm. Raman spectroscopy shows that serpentinite is composed of abundant polygonal serpentine (peak at 3697 cm^{-1} and a shoulder at 3689 cm^{-1}) and lizardite (two intense peaks at 3683 and 3703 cm^{-1}), with minor chrysotile (usually in veins, main peak at 3698 cm^{-1} with a shoulder at 3691 cm^{-1}).

Spinel from the Sabzevar host serpentinite shows two main alteration features. We will call "*partly altered Al-spinel"*, the homogenous spinel single-crystals that are partly replaced along rim and cracks by a secondary spinel matrix containing voids filled with magnetite + Al-bearing hydrous silicate +/- brucite. This type of replacement texture is often called "porous" in the literature, due to the presence of (filled) voids. A second type of spinel alteration texture in the Sabzevar host serpentinite corresponds to entirely porous zones that lack any Al-spinel relict cores. This second type of texture will be called *porous Cr-spinel*, hereafter, since the dominant spinel in this textural type is Cr-rich. Porous Cr-spinel zones are strongly fractured and the average grain size is between 5 and 20 μm (Fig. 3b and 3.c). At the microscale, the porous Cr-spinel matrix seems to be replaced by patches of Fe-chromite and magnetite intergrowths (Fig. 3c), possibly indicative of a further alteration stage. Andradite occurs as skeletal masses surrounding porous Cr-spinel in serpentinites (Fig. 3d). Fe-Ni alloys are finely dispersed around spinel grains in the serpentine groundmass. Sulfide grains were not encountered in the studied serpentinite samples.

4.2 Magnetite ore

The studied Sabzevar magnetite ores are heterogeneous in texture and consist of euhedral to subhedral magnetite crystals with sizes from 5 to 500 μm (Fig. 2c). The silicate matrix is composed of serpentine (70-80 vol.%), andradite (15-20 vol.%) and minor chlorite (< 5 vol.%). Relicts of spinel surrounded by polycrystalline magnetite were found within all investigated magnetite ore samples. The texture of these relict spinels can either be porous (Fig. 3e and f) as defined for serpentinite-hosted spinel

or massive (Fig. 3g). Magnetite around porous chromite can either be small newly-formed grains (Fig. 3f) or form a thick polycrystalline rim with serpentine +/- brucite inclusions (Fig. 3e). Euhedral magnetite crystals can also be found as inclusion in andradite crystals (Fig. 3h). In a few cases, individual andradite-rich veins cut through the magnetite ore. Sulfide minerals are sporadically dispersed in the Sabzevar magnetite ores. Pentlandite, $(Fe,Ni)_9S_8$, with subordinate heazlewoodite, Ni_3S_2, and chalcopyrite are common sulfides. Pentlandite and heazlewoodite occur mainly as anhedral to subhedral inclusions with variable sizes and/or as large aggregation in magnetite crystals (Fig. 3i).

4. Mineral chemistry

4.1 Spinels

The composition of spinel from magnetite ores and from the host serpentinites have been plotted in a trivalent-cation (Fe^{3+}-Cr-Al) ternary plot as well as in binary $X_{Cr} - X_{Mg}$ and $Fe^{3+}/(Fe^{3+} + Fe^{2+}) - X_{Mg}$ diagrams (Fig. 4). The cores of partly altered Al-spinel have the lowest chromium number and the highest Al content. They display compositions that are typical for spinel from ophiolitic forearc peridotites (Fig. 4; Table S1).

In the serpentinite samples, spinels from the porous rim of partly altered Al-spinel and from porous Cr-spinel matrix share strong chemical similarities and are most likely genetically related. They both plot in the same regions of the compositional diagrams shown in Fig. 4. They are relatively depleted in Al compared to the partly altered Al-spinel and enriched in chromium relatively. Patches of porous chromite formed by transformation of the Cr-spinel porous matrix have also been plotted in Fig. 4. The composition of porous and homogeneous chromite cores in the magnetite ores strongly resembles that of Cr-spinel from the serpentinite samples (Fig. 4).

X-ray elemental maps, along with point microanalyses, were collected using the EPMA on homogeneous and porous Cr-spinel relicts rimmed by magnetite (Figs. 5 and 6), from the magnetite ore samples. The various elemental maps obtained on homogeneous chromite confirms its chemical homogeneity at the minor elements level. On a chemical basis (Table S2; Figs. 5 and 6), two generations of magnetite can be distinguished. A first magnetite rim is observed (called "magnetite-I rim") from the Cr-spinel interface, which has a thickness of ~ 20 μm and displays a SiO_2 content <1 wt.%, a Cr_2O_3 content of 2.70-3.69 wt.% and a TiO_2 content > 1 wt.%. A second magnetite rim (called "magnetite-II rim") has a variable thickness ranging from 40 to 200 μm, and shows a different composition reflecting the presence of inclusions at the nanoscale. The SiO_2 content is higher and ranges from 1.21 to 2.35 wt.%. The MgO and Cr_2O_3 contents are variable in the 0.06-0.12 wt.% and 0.03-1.62 wt.% range, respectively. The TiO_2 content is lower (< 0.47 wt.%). Titanium is heterogeneously distributed within

the magnetite-I rim, with the highest concentration close to the chromite – magnetite-I boundary. On the elemental maps, the magnetite-I/II interface is sharp and seems to outline former crystal faces. Porous chromite shows higher Al, Mn, Ni and V in comparison with homogenous chromite relicts (Table S2). Mg- and Al-rich spotty zones in porous chromite outline the numerous chlorite inclusions (Fig. 6).

4.2 Sulfides and alloys

Chemical compositions of sulfides and alloys in the Sabzevar magnetite ores and associated serpentinites are given in Table S3. Pentlandite displays a wide range of Co (7.53 - 27.12 wt.%.), Ni (18.56 - 36.67 wt.%) and Fe (17.34 - 29.96 wt.%) contents. There is no obvious relationship between composition and textural position of pentlandite. Average composition of heazlewoodite shows Ni (74.03 wt.%), S (27.37 wt.%) and Co (0.17 wt.%). Fe–Ni alloys from the Sabzevar serpentinites show a large range of compositions from $Ni_{73}Fe_{19}$ to $Ni_{80}Fe_{26}$, which can be classified as awaruite (Ni_3Fe).

4.3 Andradite, chlorite and brucite

Andradite in both magnetite ore and host serpentinite have similar chemical compositions (Table S4). They are chemically homogeneous and characterized by TiO_2 content < 0.30 wt.%, Al_2O_3 contents ranging between 0.40–1.15 wt.%, Cr_2O_3 contents between 0.04 - 1.20 wt.% and Fe_2O_3 contents between28.76 - 30.24 wt.% (Table 5). Chlorite inclusions in chromian spinels from the magnetite ores have higher FeO contents (2.55 - 5.52 wt.%) compared to those in chromian spinel from the host serpentinite (Table S5). Chlorite inclusions in chromian spinel from both magnetite ore and host serpentinite display relatively high Cr_2O_3 content (2.30 - 5.02 wt.%) and variable Al_2O_3 content (6.66 - 14.74 wt.%) (Fig. 4a). Brucite in the Sabzevar host serpentinite has X_{Mg} values ranging from 0.60 to 0.75.

5. Nanoscale characterization of the magnetite rims

A lamella was cut across at the interface between Cr-spinel with homogeneous texture and magnetite from the magnetite ore (sample MG15; black arrow in Fig. 5) for TEM characterization to gain insight on the Cr-spinel alteration processes at the nanoscale. The contact between Cr-spinel with homogeneous texture and magnetite can be divided into four zones (Fig. S2). At the lamella scale, Cr-spinel is homogeneous in composition, Al-, Cr- and Mg-rich and relatively depleted in Fe (Table S2; Fig. 7). This composition is consistent with EPMA analyses performed on the same grain (Fig. 4). It contains a few subgrain boundaries. Automatic crystal orientation mapping reveals a homogeneous orientation in Cr-spinel with a misorientation of less than 0.5° over a distance of 1 μm. STEM-EDS mapping indicates that Cr-spinel is separated from magnetite-I by a ~ 1 μm thick rim of a phase which could not be resolved with EPMA (Fig. 7a). This phase displays a Cr content similar to that of Cr-spinel

but contains lower Al and Mg and higher Fe contents (Fig. 7b to g). Such a composition recalls the composition of ferritchromite from the host serpentinite. We therefore use in the following the same nomenclature as for the host serpentinite. The contact between ferritchromite and magnetite-I is sharp on STEM-EDS maps. Locally, the contact is marked with Ti-rich lenses with sizes below 50 nm (Fig. 7f) which indicate that Ti is segregated through the precipitation of a Ti-rich phase (e.g., rutile). Bright field and HAADF images do not allow to locate the Cr-spinel – magnetite-I boundary as clearly as with STEM-EDS mapping (Fig. 7a).

The misorientation angles extracted from the orientation maps are of less than 3° and 0.5° at the Cr-spinel – ferritchromite and the ferritchromite – magnetite-I interfaces, respectively (Fig. 8a). The comparison of electron diffraction patterns (SAED) on both sides of the interface is in line with small misorientation angles. Cr-spinel and ferritchromite display coherent planes (Fig. 8b). The high resolution TEM images also show some continuous planes across the interface (Fig. 9a). The SAED patterns of ferritchromite and magnetite-I are identical, indicating perfect epitaxy (Fig. 8c).

Magnetite-I is ~ 10 µm thick in the investigated region (Fig. S2). It is homogeneous in composition and enriched in Si and Ti compared to Cr-spinel and ferritchromite. The nanostructure of magnetite-I is complex with micrometer-wide grains surrounding regions composed of densely packed 20 nm-wide grains (Fig. S3). The contact between magnetite-I and magnetite-II is sharp. The two magnetite types display similar composition (Fig. 10). Magnetite-II contains 100 nm-wide and 300 nm-long, Fe-poor and Mg- and Si-rich inclusions, probably made by serpentine. These inclusions are likely responsible for the high Si contents measured by EPMA (Figs. 4 and 5). The orientation of magnetite-I and magnetite-II is different with a misorientation angle between the two phases of 35° (Fig. 8d). This is confirmed on high-resolution images which show a steep angle between the lattice planes in magnetite-I and magnetite-II (Fig. 9b).

6. Thermodynamic modelling

Phase relationships have been calculated on the Sabzevar serpentinite composition at 500 MPa and plotted in a $\Delta\log_{10}fO_2$-T diagram (Fig. 11). Among the main features of this calculation, there is the composition of the spinel solid solution(s), $(Mg,Fe)(Al,Fe,Cr)_2O_4$, which contains two redox sensitive elements, Fe and Cr, and which is thus expected to be fO_2 dependent. Furthermore, a solvus in the $Fe(Fe,Cr)_2O_4$ spinel subsystem has been reported below ca. 550°C (Sack and Ghiorso, 1991), which is thus relevant to the temperature range investigated here. The incorporation of chromium in garnet is also accounted for by the garnet solid-solution considered here. Although chromium-bearing chlorite is also likely to share phase relationships with Cr–spinel and Cr-bearing garnet, no Cr-chlorite component has been considered in the chlorite solution used in the present calculation. Consequently, the stability field of chlorite might be larger than predicted here.

We computed the composition of the spinel solid solution(s) along a cooling path divided in two parts (Fig. 11). The oxygen fugacity in the high temperature part of the path (800 to 420°C) is internally buffered by the olivine – Mg-silicate – spinel assemblage (Frost, 1985). The low-temperature part of the path (420 to 300°C) considers a serpentinization reaction in which the amount of oxygen is fixed. The bulk rock + fluid composition is assumed to be the one of a ferrous peridotite plus pure water. Such a path provides a first-order estimate of the effect of temperature on spinel composition. At high temperature and high fO_2 (800°C and $\Delta\log_{10}fO_2 = 0$, respectively), the single spinel solid-solution contains mainly Mg as divalent cation (Fig. 12b) and ~ 60 % of Al as trivalent cation (Fig. 12a), leading to simplified composition of $Mg(Fe_{0.1},Cr_{0.3},Al_{0.6})_2O_4$. At T < 730 °C, the Al content of the spinel strongly decreases due to the formation of chlorite. As a result, the X_{Cr} of the spinel increases from 0.6 at ~730°C to > 0.95 at ~ 600°C and below. At T < 400°C, two spinels are predicted to form in association with brucite, $(Mg,Fe)(OH)_2$. The first type of spinel has a composition close to that of the high temperature spinel. Its $Cr/(Cr+Fe^{3+})$ ratio progressively increases from ~ 85% at 400°C to 95 % at 350 °C leading to an $Mg(Fe_{0.05},Cr_{0.95})_2O_4$ composition. The second type of spinel is close to the magnetite end-member since it contains mainly Fe^{3+} as trivalent cation and Fe^{2+} as divalent one. The formation of this near-endmember magnetite occurs at the expense of olivine through serpentinization reactions (Fig. 11). The amount of Mg among the divalent cations decreases from 70 down to 0 mol.% from 430 to 300 °C, respectively. Simultaneously, the molar fraction of brucite in the solid increases from 6 to 84 mol.% (0.1 to 5.9 wt.%; Fig. S4).

The composition of the aqueous solution has also been calculated for the same bulk-rock composition and in the same $\Delta\log_{10}fO_2$ – T range. The pH is slightly alkaline at low temperatures, as expected for water interacting with an ultramafic lithology (Galvez et al., 2016). It decreases with temperature from 2.5 pH units above neutral at 250°C to 0.5 pH units above neutral at 800°C. The fraction of H_2 in the solvent increases as the temperature increases and as the oxygen fugacity decreases . The concentration of dissolved iron is rather constant around 10^{-3} mol/kg along the cooling path investigated here (Fig. 13 a). The dominant iron-bearing aqueous species are ferrous iron species. $HFeO^{2-}_{,aq}$ dominates at T below 500 °C whereas $Fe(HSiO_3)^+$ dominates above 500 °C. Chromium solubility is between 7 and 8 orders of magnitude lower than iron solubility (Fig. 13 b, Fig. S5 and S6). Therefore, Cr must be considered as an insoluble element in the conditions investigated here. The Cr aqueous species are dominated by trivalent chromium species, Cr(III), at relatively low oxygen fugacity with Cr(III)/(Cr(II) + Cr(III) + Cr(VI)) > 99% in most of the investigated $\Delta\log_{10}fO_2$ – T domain. Among the Cr(III) species, $Cr(OH)_{4,aq}^-$ dominates. Cr solubility is approximately one order of magnitude higher at temperatures above 500 °C than at low temperature along the cooling path investigated here.

7. Discussion

7.1 Two-stage spinel alteration process

Three types of spinel were identified based on their microtexture and composition in the serpentinite hosting the magnetite ores. We described the first type of microtexture as *partly altered spinel,* which consists in a *homogeneous* Al-Cr spinel core (X_{Cr} of 0.6). The Al-Cr spinel core composition falls at the end of the compositional range of magmatic spinels reported in the Sabzevar ophiolite podiform chromitite deposits (Fig. 4), which derived from island arc tholeiites with boninitic affinity (Shafaii Moghadam et al., 2015; Eslami et al. 2018b). Both textural relationships and composition suggest that the Al-Cr spinel core in the partly altered type is a relict of magmatic spinel that was possibly altered during magmatic processes. The magmatic part of the spinel history will however not be discussed here. We will consider that these residual cores correspond to a first generation of spinel and will thus be named (Cr,Al)-spinel-I in the following.

(Cr,Al)-spinel-I is partly replaced along rim and cracks by a *porous rim* composed of a secondary Cr-spinel, or Cr-spinel-II, matrix (X_{Cr} of= 0.8) containing voids partially stuffed with Al-bearing hydrous silicate +/- brucite. Besides the partly altered texture, other spinel-rich areas are found which are, texturally, entirely porous (i.e., with no homogeneous core). Cr-spinel-II of the porous rim of partly altered spinel and the spinel that composes the matrix of those fully porous areas have also similar compositions. This suggests that these two spinel types are genetically related. The absence of a homogeneous core in that case is interpreted as the result of the complete replacement of (Cr,Al)-spinel-I leaving no relict behind in contrast to partly altered (Cr,Al)-spinel textures. Therefore, we did not distinguish between the secondary Cr-spinels (Cr-spinel-II) in both textural types.

At the micrometer scale, the chromite found in the magnetite ore displays two types of microtextures. They are either anhedral with a homogeneous composition (Fig. 5) or made by an aggregate of subgrains leading to a porous microtexture (Fig. 6). The homogenous spinel grains are surrounded by a magnetite rim, whereas such a rim is not systematically found around porous chromite in the magnetite ores. The regions where rims are not found are strongly deformed. This may indicate cataclasis, leading to a loss of the microtextural information necessary to link chromite and magnetite formations. All chromite grains have identical composition similar to Cr-spinel-II from the host serpentinite (Fig. 4). Moreover, some of them display a similar porous texture. Therefore, their formation probably originates from the reaction of the same type of magmatic spinels as in the serpentinite host. In that respect, we tentatively categorized them as Cr-spinel-II as well, even though, we did not find patches of magnetite and/or ferritchromite in the porous chromite found in the magnetite ores. Indeed, magnetite only occurs as a rim around the Cr-spinel-II core either homogeneous or porous. A ~ 1 µm thick spinel phase separates Cr-spinel-II from a first magnetite rim (magnetite-I). Its composition is consistent with the ferritchromite analyses collected in the serpentinite (Al, Mg and Fe

contents intermediary between magnetite and Cr-spinel-II; Fig. 6). Ferritchromite and magnetite display a perfect epitaxial relationship, suggesting mutual growth during the same alteration stage at the expense of Cr-spinel-II. This type of pseudomorphic replacement of Cr-spinel-II can be considered as an indicator of replacement during a dissolution-precipitation process following Putnis (2002). The misorientation of only few degrees measured at the contact between Cr-spinel-II and ferritchromite is thus interpreted as evidence for replacement of Cr-spinel-II by an assemblage composed of magnetite and ferritchromite.

The microtextural and compositional information point thus towards spinel alteration sequence proceeding in two stages. The magmatic spinel, (Cr,Al)-spinel-I, is first replaced during alteration "Stage I" by a porous chromite, Cr-spinel-II, containing chlorite inclusions, which then reacted during alteration "Stage II" to form magnetite and ferritchromite. This alteration sequence occurred in both the host serpentinite and the magnetite ore. However, the spatial relationship (patches or reaction rims) and the fraction of ferritchromite (high or restricted to a thin layer) differ between the two lithologies. Thermodynamic modelling is used in the following to constrain the temperature and oxygen fugacity having prevailed during the two aforementioned stages of alteration.

7.2 Conditions prevailing during the alteration stages

Thermodynamic modelling has been used in the past to predict the evolution of spinel composition as a function of temperature. Gervilla et al. (2012) were able to predict the evolution of the spinel X_{Cr} during alteration from the spinel solid solution model proposed by Klemme et al. (2009). Colas et al. (2019) calculated the evolution of the spinel X_{Mg} with another solid-solution model based on the ideal solid solution between Mg and Fe^{2+} on the tetrahedral site as proposed by Engi (1983). These solid solutions either ignore ferric end-members (magnetite, $FeFe^{3+}{}_2O_4$, and magnesioferrite, $MgFe^{3+}{}_2O_4$) or they consider ideal mixing between end-members. This has only minor consequences on calculated high-temperature spinel compositions since spinel is Fe^{3+}-poor at high temperature. However, the consideration of ideal mixing precludes for instance the prediction of the immiscibility gap between magnetite and ferritchromite which is encountered towards low temperatures. We circumvented this problem by introducing the mixing parameters of Sack and Ghiorso (1991) in a reciprocal solid-solution model in Perple_X (Supplementary Materials 1). Thermodynamic modelling with this latter solid-solution model in the Cr-CFMASH system with the composition of the Sabzevar serpentinite provides insights on the temperature – $\Delta\log_{10}fO_2$ conditions prevailing during spinel alteration.

According to our thermochemical modelling, the composition of chromite is very sensitive to temperature and $\Delta\log_{10}fO_2$, as suggested by Evans and Frost (1976). Simulation of spinel composition during a cooling path from 800 down to 300 °C (500 MPa) associated with an increase from 0 to 2 followed by a decrease from 2 to -4 in $\Delta\log_{10}f_{O2}$, shows that the chromite composition drastically

changes at ~ 700 and ~ 450 °C (Fig. 12). At temperature above ~ 700 °C, a magmatic spinel-like composition is obtained with an X_{Cr} of 0.4 slightly higher than in the natural samples and an X_{Mg} close to 1 (Fig. 12). Below ~ 700 °C, X_{Cr} rapidly increases due to the formation of chlorite which incorporates aluminum. The silica necessary to form chlorite is provided by olivine and orthopyroxene. This predicted evolution of the spinel composition is in good agreement with the evolution occurring in the course of alteration "Stage I" as observed in the Sabzevar samples where porous Cr-spinel-II containing chlorite inclusions has formed at the expense of (Cr,Al)-spinel-I. Thermodynamic modelling constrains the alteration "Stage I" to temperatures and $\Delta \log_{10} fO_2$ comprised between 575 and 725 °C and 0 and 3, respectively. Based on thermodynamic modelling and the composition measured in the Sabzevar samples, the following reaction is proposed for "Stage I":

$$133\ (Mg_{0.64}Fe_{0.36})(Cr_{0.6}Al_{0.4})_2O_4 + 70\ (Mg_{0.9}Fe_{0.1})_2SiO_4 + 86\ (Mg_{0.9}Fe_{0.1})SiO_3 + 208\ H_2O + 9\ O_2 = 90\ (Mg_{0.4}Fe_{0.6})(Cr_{0.8}Fe_{0.1}Al_{0.1})_2O_4 + 26\ (Mg_{9.7}Fe_{0.3}Al_{1.4}Cr_{0.6})Al_2Si_6O_{20}(OH)_{16} \quad (1)$$

Magmatic spinel + olivine + orthopyroxene + water + oxygen = Cr-spinel II + chlorite

The source of oxygen in the system is difficult to infer from the data and could be primary mineral reduction (pyroxene) or water dissociation. The reaction of one mole of magmatic spinel requires at least 1.2 times more moles of olivine and orthopyroxene to reach completion. Merlini et al. (2009) used image analysis on mineral assemblages having recorded a reaction similar to Reaction (1). They found a correlation between the volume of silicates initially present and the extent of reaction. This observation indicates that reaction progress depends on silica availability rather than on kinetics. In the Sabzevar ophiolite, the olivine + orthopyroxene over magmatic spinel amount ratio is much higher in the serpentinite than in the magnetite ore. However, magmatic spinel is only preserved in the serpentinite, suggesting that silica availability does not control reaction progress alone. The silica source to form chlorite is derived from olivine and orthopyroxene in Reaction (1) rather than antigorite as proposed by Merlini et al. (2009). This has fundamental implications for the inference of possible alteration scenarios. In the thermodynamic simulation provided here, the chlorite stability field can be entered either through cooling and olivine/orthopyroxene breakdown (retrograde metamorphism) or through heating and antigorite breakdown (prograde metamorphism). We found that the samples of the Sabzevar ophiolite experienced two alteration stages with first the production of Cr-spinel II at the expense of (Cr,Al)-spinel I and then the development of a reaction rim composed of Fe-chromite ($FeCr_2O_4$) and magnetite (Fe_3O_4) around Cr-spinel II. Thermodynamic modelling predicts that alteration Stage I occurs at approximately 650 °C and alteration Stage II below 430 °C (Figs 11 and 12). The reaction sequence observed here thus proceeded upon cooling.

The thermodynamic simulation also predicts the formation of brucite during alteration "Stage II", in agreement with the observations in the serpentinite from the Sabzevar ophioliteFig. S7. Mg depletion from spinel is compensated through ferric iron reduction to form magnetite according to the

following reaction based on the compositions measured in the Sabzevar samples (in which Al is not considered for simplicity):

$$60\ (Mg_{0.4}Fe_{0.6})(Cr_{0.85}Fe_{0.15})_2O_4 + 16\ H_2O + 8\ H_2 = 51\ FeCr_2O_4 + Fe_3O_4 + 24\ Mg(OH)_2 \quad (2)$$

Cr-Spinel II + water + dihydrogen = ferritchromite + magnetite + brucite end member

Reaction 2 is fO_2 dependent and is favored by reducing conditions, i.e., higher H_2 partial pressures. This is consistent with the thermodynamic modelling which indicates that the serpentine + brucite + ferritchromite + magnetite assemblage is only stable at $\Delta\log_{10}fO_2$ below 2. Serpentinization of olivine during mantle-rock alteration is known to produce H_2 in the same temperature range as reaction (2) (McCollom and Bach, 2009). It leads to extremely reducing conditions favoring the precipitation of Fe-Ni alloys (e.g., awaruite; Frost, 1985; Klein and Bach, 2009). We observed awaruite as tiny grains (<2 μm) close to Cr-spinel-II crystals in the serpentinites of the Sabzevar ophiolite (Fig. S8), suggesting that the reducing conditions imposed by serpentinization promoted Reaction (2) below ~ 400°C.

Reaction (2) produces a volume of ferritchromite which is 57 times larger than the volume of produced magnetite assuming isochemical conditions. This is not consistent with our observation of the magnetite ore where ferritchromite rims are approximately two orders of magnitude thinner than the magnetite rims. This implies that alteration "Stage II" is not isochemical in the magnetite ore and it should involve either Cr depletion or Fe addition. Alteration "Stage II" thus occurred under open system conditions with mass transfer at least over the size of the magnetite ore bodies (> 0.5 m). We use in the following the observed microtextures to provide additional constraints on the mobility of these two elements.

7.3 Chromite microtexture formation and element mobility

The formation of hydrous phases (chlorite, serpentine and brucite) during spinel alteration implies the presence of an aqueous fluid. Dissolution-precipitation occurring at the mineral interfaces is an efficient process to promote metamorphic reactions and mineral replacement reaction (Putnis and Austrheim, 2010). This type of process will be favored to interpret spinel alteration in the Sabzevar ophiolite.

Our dataset indicates that Cr-spinel-II either forms a porous texture or homogeneous grains. Based on the preservation of magmatic spinel cores rimed by porous Cr-spinel-II, the development of Cr-spinel-II porous textures seems to imply the inward migration of the magmatic spinel – fluid boundary accompanied by the in-situ precipitation of the secondary products (mainly Cr-spinel-II and chlorite) at constant Cr and Al content. Cr, which is present as Cr(III), and Al display both low concentration and low diffusivity, they are thus expected to be mostly immobile. Note that this general

scheme does not apply if ligands that will complex Al and Cr are present (Huang et al., 2019). These aqueous species have not been considered in our thermochemical modelling. We do not see an indication for such complexation and suggest that the formation of porous textures is controlled by dissolution-precipitation reactions and the limited mobility of Cr and Al compared to that of aqueous Si, Fe and Mg.

The assumption of low Cr and Al mobility used to explain porous replacement textures is challenged by the fact that Cr-spinel-II can also be present as homogeneous area with a size up to 20 μm, with no obvious co-precipitation features.

Owing to the large temperature range estimated for alteration "Stage II", these larger Cr-spinel-II grains may have formed at the highest temperatures under which diffusive transport is more efficient. Cr and Al transport over larger distances (sub-cm scale) may have been enhanced locally by advection channels. Species transport may also depend on the initial microstructure of the (Al,Cr)-spinel-I which seems to be highly variable in podiform chromitites (Leblanc, 1980).

Alteration "Stage II" in the serpentinite preserves the patchy texture with small Fe-chromite and magnetite grains locally growing at the expense of Cr-spinel-II. In the magnetite ore, such a patchy texture is not encountered since Fe-chromite and magnetite are not found as isolated grains but rather as continuous rims surrounding the entire homogeneous or porous Cr-spinel II grains (Fig. 3, 5 and 6). Such a difference in microtexture may be inherited from the alteration "Stage I" during which homogeneous grains were more prone to form in the magnetite ore than in the serpentinite. The porous texture may favor fluid access and chemical exchange in the serpentinite in comparison to the less permeable homogeneous texture found in the magnetite ore. In the magnetite ore, the successive occurrence of Cr-spinel-II, Fe-chromite and magnetite from the grain center to the rim recalls previous observations in altered ultramafic rocks (Ulmer, 1974; Wylie et al., 1987; Michailidis, 1990; Prabhakar and Bhattacharya, 2013; Barra et al., 2014; Colas et al., 2019). Prabhakar and Bhattacharya (2013) interpreted the formation of ferritchromite as a result of intercrystalline diffusion between Cr-spinel-II and magnetite formed during serpentinization. The changes in composition observed here at the Cr-spinel-II – ferritchromite and ferritchromite – magnetite interfaces are sharp, even at the nanoscale, which is inconsistent with diffusion (Fig. 7 and 8). Ulmer (1974) observed a similar texture but with a larger ferritchromite rind and thus also ruled out a diffusion process based on the same textural argument. The interpretation of Prabhakar and Bhattacharya (2013) was based on the fact that the magnetite outer rim does not mimic the Cr-spinel-II rim, as it would be expected for a replacement reaction (Putnis, 2002). We observed the same digitized outer rim of magnetite here. However, based on elemental X-ray maps (Fig. 5 and 6), collected on the magnetite rim, two distinct magnetite generations of different composition can be distinguished. The first type (magnetite-I) in contact with ferritchromite is Si-poor and Ti- and V-rich. Magnetite-I is surrounded by a second magnetite generation (magnetite-II). The interface between magnetite-I and magnetite-II is sharp and angular and mimics the

588 shape of Cr-spinel-II. Pseudomorphic replacement is confirmed by the small misorientation between Cr-
589 spinel-II and ferritchromite across their common interface. These observations indicate that
590 ferritchromite and magnetite-I are formed through a replacement process (Wylie et al., 1987) during
591 alteration Stage II. The spatial distribution of ferritchromite and magnetite suggests the presence of
592 chemical potential gradients during precipitation. As for alteration "Stage I", the calculated Cr solubility
593 is low and the dissolved Cr species are trivalent during alteration "Stage I". Fe is mainly divalent and
594 several orders of magnitude more soluble than Cr. This promotes slow and fast Cr and Fe transports,
595 respectively. As a result, a strong chemical potential gradient in Cr_2O_3 is expected to develop during the
596 alteration of the Cr-spinel-II whereas the chemical potential gradient in FeO, if any, is expected to be
597 smooth. This generates a supersaturation in ferritchromite only in the vicinity of Cr-spinel-II. The small
598 thickness of ~ 1 μm measured here for the ferritchromite indicates that Cr was almost immobile during
599 the alteration and that the dissolution of Cr-spinel-II was extremely slow, in agreement with the low
600 temperature inferred for alteration "Stage II". In such conditions, the initial surface of the Cr-spinel-II
601 grain is expected to be close from the actual position of the ferritchromite – magnetite contact. The
602 presence of ferritchromite with a crystal structure and unit-cell parameters similar to magnetite can be
603 used as a template for magnetite growth. Such an epitaxial growth of magnetite on ferritchromite is
604 energetically favored since it circumvents the need for nucleation (Fig. 8). The observation of a second
605 magnetite type (magnetite-II), with no orientation relationship with ferritchromite and magnetite-I
606 suggests that magnetite could also precipitate in the serpentine/chlorite matrix during the alteration
607 "Stage II" (Fig. 8 and 9). The differences in composition measured at the micrometer scale between
608 magnetite-I and magnetite-II is no longer observed at the nanometer scale but Ti-rich and silicate
609 inclusions have been found in magnetite-I and -II, respectively (Fig. 10; Deditius et al., 2018).
610 Magnetite-I does not contain silicate inclusions but displays a silica content of ~ 1.23 wt.% (Fig. 5 and
611 10), indicating that Si is also incorporated in the magnetite structure. As a result, the micrometer-scale
612 difference in composition between magnetite-I and magnetite-II does not necessary reflect a difference
613 in fluid composition or temperature during precipitation. It rather indicates different growth mechanisms
614 (pseudomorphism or not) and different locus of precipitation (Cr-spinel II surface or silicate-rich
615 matrix). Silican magnetite has been reported in a wide range of rocks including ultramafic rocks, igneous
616 rocks and banded iron formations (Huberty et al., 2012 and references therein). Ciobanu et al. (2019)
617 have recently reported pseudomorphic rutile inclusions and Mg-bearing silicate inclusions in magnetite,
618 similar to the one reported here.

619 **7.4 Iron mobility and magnetite ore formation**

620 Several genetic processes have been invoked for the genesis of serpentinite-hosted magnetite
621 deposits: (i) precipitation from a high-temperature (~300–400 °C) fluid in a hydrothermal system (e.g.
622 Toffolo et al., 2017.; Khedr and Arai, 2018) ; (ii) low-*T* (100–300 °C) serpentinization at high water-
623 rock ratio (e.g. Gahlan et al., 2006; Eslami et al., 2018a); and (iii) metamorphic transformation of pre-

existing chromitite with magmatic origin into magnetite (e.g. Paraskevopoulos and Economou, 1980; Rossetti et al., 2009).

The dataset presented here provides additional important constraints on the formation of magnetite ore bodies. Magnetite-I and magnetite-II are formed here during alteration "Stage II" at temperature below 430 °C and in reducing conditions (oxygen fugacity below the FMQ buffer). These conditions are compatible with serpentinization during which the iron initially contained in olivine and pyroxene is incorporated as Fe^{2+} in serpentine and brucite or oxidized and incorporated as Fe^{3+} in magnetite and serpentine (McCollom et al., 2009). The distribution of iron between the reaction products is mainly controlled by temperature, with magnetite being the main iron carrier at temperature above 200 °C (Klein et al., 2009; Malvoisin et al., 2012; Klein et al., 2014). The first magnetite grains formed in hydrothermal processes such as early serpentinization, are likely nano-sized and thus highly reactive (Brunet, 2019). Bach et al. (2006) and Beard et al. (2009) found in serpentinites from the Mid-Atlantic Ridge that iron first precipitates in brucite in the core of the meshes formed during olivine serpentinization. Also, submicrometer magnetite grains have been observed in similar mesh cores observed in natural samples (Rouméjon et al., 2018; Liu et al., 2019; Malvoisin et al., 2020). Iron is then re-mobilized during the dissolution of brucite or tiny magnetite grains and transported out of the center and towards the border of the meshes where magnetite precipitates. Maffione et al. (2014) used magnetic and petrographic data to show that nanograins of magnetite are formed in the incipient stages of serpentinization. The grain size then increases to reach several micrometers at higher serpentinization degrees. Malvoisin and Brunet (2014) reported the formation of both submicrometer and tens of micrometer-wide magnetite grains during experiments of dunite serpentinization. Iron is thus transported at least at the hundreds of micrometer scale during serpentinization.

Alteration "Stage II" in the magnetite ore provides constraints on the extent of iron mobility during serpentinization. This stage should indeed produce 57 more ferritchromite than magnetite in volume if the reaction was occurring in a closed system according to Reaction (2). This proportion is at odds with the observed 50 to 100 µm-wide rim of magnetite-I + magnetite-II and 1 µm-thick rind of ferritchromite at the Cr-spinel II surface. Such a phase proportion requires a pronounced mass transfer between the magnetite ore body and its surrounding, most likely the host serpentinite. We showed above that Cr is immobile and Fe is the main element to be transferred to the magnetite ore. Fe probably originated from direct transport of the Fe^{2+} produced during olivine dissolution or from the dissolution of nanosized magnetite grains initially formed in the host serpentinite during early serpentinization (Brunet, 2019). Thermodynamic modelling reveals that the iron content measured in the Sabzevar serpentinite is too low to reproduce the Mg/(Mg+Fe) ratio measured in olivine relicts, suggesting that iron is lost in the peridotite during alteration. Iron transfer requires an iron chemical potential gradient between the host serpentinite and the magnetite ore. Such a gradient can be generated if the energetic barrier to overcome for magnetite precipitation is lower in the magnetite ore than in the serpentinite

host. Three processes can contribute to reduce the energetic barrier at the spinel surface. As discussed above, the similarities in crystal structure first allow for an epitaxial growth of magnetite over Cr-spinel -II without a need for nucleation (Fig. 9). The growth of the tens of micrometer-wide spinel grains in the magnetite ore is also favored by their smaller interfacial energy compared to the nanograins of magnetite formed during serpentinization (Ostwald ripening). Magnetite formation during serpentinization also requires electron transfer from Fe^{2+} to water, leading to water splitting and H_2 formation. Spinel-structure minerals have been proposed to catalyze this process (Mayhew et al., 2013) due to the high mobility of electrons in their structure (Hamilton, 1958; Skomurski et al., 2010) and to the possibility to sorb water at the spinel surface (Kendelewicz et al., 2000; Parkinson et al., 2011).

We aim in the following at calculating the amount of olivine necessary to form the magnetite ore bodies observed in the Sabzevar ophiolite. On the two-dimensional outcrop, magnetite ore bodies occur as boudins with a thickness of L_{ore} ~ 0.5 m hosted in a serpentinite. We assume in the following that the thickness of the magnetite ore is also ~ 0.5 m in the third direction, that the serpentinite was initially a dunite composed of olivine (Fo_{90}) and that all the iron initially contained in olivine has been transported up to the magnetite ore according to a simplified reaction: $2(Mg_{0.9}, Fe_{0.1})_2SiO_4 + 2.2\ H_2O + 0.8\ H^+ => Mg_3Si_2O_5(OH)_4 + 0.6\ Mg(OH)_2 + 0.4\ Fe^{2+}_{,aq}$. This latter reaction implies that, in the host-serpentinite, no Fe is incorporated into lizardite and brucite and that no magnetite is formed. Under these assumptions, the minimum thickness of dunite necessary to form the ore bodies can be expressed as:

$$Ldun = \frac{3\nu LoreVmol}{2XFeVmmag} \quad (3)$$

where ν is the volume fraction of magnetite in the ore bodies (90 vol. %) and V_{mol} and V_{mmag} are the molar volume of olivine and magnetite, respectively ($Vmol = 44.73c\,m^3/mol$ and $Vmmag = 44.56c\,m^3/mol$). Equation (3) leads to an estimated dunite thickness of 6.8 m. This estimate is a minimum, as it is assumed that all iron is lost from the dunite. The bulk iron content measured in the Sabzevar serpentinite is around 20 % lower than the amount necessary to reproduce the measured olivine composition with our thermodynamic modelling. Considering such a Fe loss would lead to a dunite thickness of ~30 m. Iron transport at a scale > 10 m requires, in addition to the chemical potential gradient in iron, an efficient transport mechanism. We observe shear zones in the magnetite ore but not in the host serpentinite, suggesting that advection cannot explain alone iron transfer. The diffusivity of Fe^{2+} in a free fluid at 300°C and 100 MPa is $\underline{D}$ ~ 10^{-8} m^2/s (Oelkers and Helgeson, 1988). It can be used to calculate a characteristic time for diffusion (τ) over a distance x = 10 m of $\tau = \frac{x^2}{D} = 300$ yr. This duration is a lower bound for diffusive iron transport as diffusion is slower at grain boundary than in a free fluid. Nevertheless, it indicates that diffusion is a possible mechanism for the observed segregation of iron.

The mechanism of magnetite ore formation proposed here involves limited chromium transport and chromite dissolution. As a result, the current amount of chromite in the magnetite ore is probably similar to the amount of chromite before alteration. Chromite now represents approximately 5 vol.% of the magnetite ore. This corresponds to a thickness of 2.5 cm for a pure chromitite layer. The chromitite was probably not exclusively composed of chromite but rather occurred as a disseminated chromitite.

8. Scenario of spinel alteration – magnetite formation

Based on textural observation at micro- and nano-scales, as well as thermodynamic modelling, the Sabzevar magnetite ores and their host serpentinites are shown to have recorded two events of spinel alteration (Fig. 14). The presence of a non-metamorphic volcanogenic massive-sulfide (VMS) mineralization, and sea-floor alteration recorded in basaltic sequences of the Sabzevar ophiolite precludes the possibility of high-grade obduction-related metamorphism in the area. A first stage of alteration is ascribed to the formation of porous Cr-spinel II with chlorite inclusions at the expense of magmatic spinel. Temperatures and $\Delta \log_{10} fO_2$ of alteration "Stage I" obtained using our new thermodynamic modelling range between 725 and 575 °C and between 0 and 3, respectively. These conditions are compatible with high-temperature hydrothermal circulation of seawater at mid-ocean ridges at depth, as suggested by Tao et al. (2020) and Hasenclever et al. (2014). A second stage of alteration is marked by the development of a reaction rim consisting of ferritchromite ($FeCr_2O_4$), magnetite (Fe_3O_4) and brucite at the expense of porous Cr-spinel-II at temperatures below 400 °C and $\Delta \log_{10} fO_2 < -2$. This reaction is fO_2 dependent and favored by the presence of H_2. The second alteration stage is interpreted as the serpentinization of the Sabzevar oceanic peridotite during progressive exhumation of mantle peridotite and associated chromitite ore deposits. Therefore, unless additional geochemical data are collected to constrain with origin of the alteration aqueous fluid, we favor a simple geodynamic scenario of seawater/rock interaction during progressive exhumation of a mantle segment including chromitite bodies to account for the spinel alteration and the formation of the Sabzevar magnetite orebodies. Although there are no structural data on the study area, re-activation of oceanic faults can be expected for the remarkable hydrothermal alteration of chromitite bodies and associated peridotites in the study area. Low modal abundances of Cr-spinel relicts in the Sabzevar magnetite ore revealed that they may derive from disseminated chromitite protoliths during these two stages of spinel alteration.

9. Concluding remarks

The main conclusions of this study can be summarized as follows:

- Sabzevar magnetite ores and their host serpentinites recorded two events of spinel alteration.

- The first alteration stage occurred at temperatures between 725 and 575 °C and led to chlorite and Al-free Cr-spinel formation.
- The second alteration stage occurred during serpentinization at temperature < 400 °C and is associated with magnetite precipitation.
- The two alteration stages probably successively occurred during mantle-rock exhumation from depth at a mid-ocean ridge.
- During spinel alteration and magnetite ore formation, chromium mobility is extremely low and chromite dissolution is limited.
- Orientation mapping at the nanoscale reveals epitaxial growth of ferritchromite and magnetite on Cr-spinel II. This is interpreted as evidence for a coupled Cr-spinel II dissolution-ferritchromite + magnetite precipitation process.
- Olivine breakdown and/or dissolution of nanoscale magnetite grains initially formed in the host serpentinite provided the iron necessary for magnetite ore formation.
- Mass balance calculations indicate iron transport over distances beyond 10 meters during serpentinization.

References

Barra F, Gervilla F, Hernández E, Reich M, Padrón-Navarta JA, González-Jiménez JM (2014) Alteration patterns of chromian spinels from La Cabaña peridotite, south-central Chile. Mineral Petrol 108(6): 819-836.

Beard JS, Frost BR, Fryer P, McCaig A, Searle R, Ildefonse B, Zinin P, Sharma SK (2009) Onset and progression of serpentinization and magnetite formation in olivine-rich troctolite from IODP Hole U1309D. J Petrol 50(3): 387-403.

Brunet F (2019) Hydrothermal production of H_2 and magnetite from steel slags: a geo-inspired approach based on olivine serpentinization. Front Earth Sci 7: 17.

Colás V, González-Jiménez JM, Camprubí A, Proenza JA, Griffin WL, Fanlo I, O'Reilly SY, Gervilla F, González-Partida E (2019) A reappraisal of the metamorphic history of the Tehuitzingo chromitite, Puebla state, Mexico. Int Geol Rev 61(14): 1706-1727.

Ciobanu CL, Verdugo-Ihl MR, Slattery A, Cook NJ, Ehrig K, Courtney-Davies L, Wade BP (2019) Silician magnetite: Si–Fe-Nanoprecipitates and other mineral inclusions in magnetite from the Olympic dam deposit, South Australia. Minerals 9(5): 311.

Deditius AP, Reich M, Simon AC, Suvorova, A, Knipping J, Roberts MP, Rubanov S, Dodd A, Saunders M (2018) Nanogeochemistry of hydrothermal magnetite. Contrib Mineral Petrol 173: 46. https://doi.org/10.1007/s00410-018-1474-1.

Dick HJ. Bullen T (1984) Chromian spinel as a petrogenetic indicator in abyssal and alpine-type peridotites and spatially associated lavas. Contrib Miner Petrol 86(1): 54-76.

Engi M (1983) Equilibria involving Al-Cr spine: Mg-Fe exchange with olivine. Experiments, thermodynamic analysis, and consequences for geothermometry. Am J Sci 284-A, 29-71.

765 Eslami A, Arai S, Miura M, Mackizadeh MA (2018a) Metallogeny of the mantle-hosted magnetite ores
766 of the Nain ophiolite, Central Iran: implications for high mobility and re-concentration of Fe promoted
767 by multi-episodic serpentinization. Ore Geol Re 95: 80-694.
768
769 Eslami A, Grieco G, Davoudi M (2018b) Preliminary geochemical studies of podiform chromitites in
770 the Cheshmeh-Khan Mining District, central sector of Sabzevar ophiolite belt, NE Iran. 8th
771 Geochemistry Symposium (2018), Antalya, Turkey.
772
773 Frost BR (1985) On the stability of sulfides, oxides, and native metals in serpentinite. J Petrol 26(1): 31-
774 63.
775 Gahlan HA, Arai S (2007) Genesis of peculiarly zoned Co, Zn and Mn-rich chromian spinel in
776 serpentinite of Bou-Azzer ophiolite, Anti-Atlas, Morocco. J Mineral Petrol Sci 102: 69-85.
777 Gahlan HA, Arai S, Ahmed AH, Ishida Y, Abdel-Aziz YM, Rahimi A (2006) Origin of magnetite veins
778 in serpentinite from the Late Proterozoic Bou-Azzer ophiolite, Anti-Atlas, Morocco: An implication for
779 mobility of iron during serpentinization. J Afrian Earth Sci 46: 318–330.
780 Galvez ME, Manning CE, Connolly JAD, Rumble D (2015) The solubility of rocks in metamorphic
781 fluids: A model for rock-dominated conditions to upper mantle pressure and temperature. Earth Planet
782 Sci Lett 1: 1–13, doi:10.1016/j.epsl.2015.06.019.
783 Galvez ME, Connolly JA, Manning CE (2016) Implications for metal and volatile cycles from the pH
784 of subduction zone fluids. Nature 539(7629): 420-424.
785 Gervilla F, Padrón-Navarta JA, Kerestedjian T, Sergeeva I, González-Jiménez JM, Fanlo I (2012)
786 Formation of ferrian chromite in podiform chromitites from the Golyamo Kamenyane serpentinite,
787 Eastern Rhodopes, SE Bulgaria: a two-stage process. Contrib Miner Petrol 164(4): 643-657.
788 Hamilton W (1958) Neutron diffraction investigation of the 119K Transition in Magnetite. Phys Rev
789 110: 1050–1057.
790 Hasenclever J, Theissen-Krah S, Rüpke LH, Morgan JP, Iyer K, Petersen S, Devey CW (2014) Hybrid
791 shallow on-axis and deep off-axis hydrothermal circulation at fast-spreading ridges. Nature
792 508(7497):508-12. doi: 10.1038/nature13174. PMID: 24759413.
793 Holland TJB, Powell R (2011) An improved and extended internally consistent thermodynamic dataset
794 for phases of petrological interest, involving a new equation of state for solids. J Metamorph Geol 29:
795 333–383, doi:10.1111/j.1525-1314.2010.00923.x.
796 Holland TJB, Powell R (1998) An internally consistent thermodynamic data set for phases of
797 petrological interest. J Metamorph Geol 16: 309–343, doi:10.1111/j.1525-1314.1998.00140.x.
798 Holland T, Powell R (1996) Thermodynamics of order-disorder in minerals; II, Symmetric formalism
799 applied to solid solutions. Ame Miner 81: 1425–1437.
800 Huang J, Hao J, Huang F, Sverjensky DA (2019) Mobility of chromium in high temperature crustal and
801 upper mantle fluids: Geochem Perspect Lett 12:1–6, doi:10.7185/geochemlet.1926.
802 Huberty JM, Konishi H, Heck PR, Fournelle JH, Valley JW, Xu H (2012) Silician magnetite from the
803 Dales Gorge member of the Brockman iron formation, Hamersley Group, Western Australia. Am
804 Miner 97(1): 26-37.
805 Kendelewicz T, Liu P, Doyle CS, Brown Jr GE, Nelson EJ, Chambers SA (2000) Reaction of water with
806 the (100) and (111) surfaces of Fe3O4 . Surf Sci 453: 32–46.

Khedr MZ, Arai S (2018) Composite origin of magnetite deposits hosted in Oman peridotites: Evidence for iron mobility during serpentinization. Ore Geol Rev 101: 180–198. https://doi-org.gaelnomade-1.grenet.fr/10.1016/j.oregeorev.2018.07.003.

Kimball KL (1990) Effects of hydrothermal alteration on the compositions of chromian spinels. Contrib Miner Petrol 105(3): 337-346.

Klemme S, Ivanic TJ, Connolly JAD, Harte B (2009) Thermodynamic modelling of Cr-bearing garnets with implications for diamond inclusions and peridotite xenoliths: Lithos 112: 986–991, doi:10.1016/j.lithos.2009.05.007.

Klein F, Bach W (2009) Fe–Ni–Co–O–S phase relations in peridotite–seawater interactions. J Petrol 50(1): 37-59.

Klein F, Bach W, Jöns N, McCollom T, Moskowitz B, Berquó T (2009) Iron partitioning and hydrogen generation during serpentinization of abyssal peridotites from 15 N on the Mid-Atlantic Ridge. Geochim Cosmochim Acta 73(22): 6868-6893.

Klein F, Bach W, Humphris SE, Kahl WA, Jöns N, Moskowitz B, Berquó TS (2014) Magnetite in seafloor serpentinite—Some like it hot. Geology 42(2): 135-138.

Klemme S, Ivanic TJ, Connolly JAD, Harte B (2009) Thermodynamic modelling of Cr-bearing garnets with implications for diamond inclusions and peridotite xenoliths. Lithos 112:986–991.

Liu ZB, Li JC, Zhao T, Song Y, Yuan GL, Lin Y, Shao HS (2020) Serpentinisation and magnetite formation in the Angwu ultramafic rocks from the central Bangong–Nujiang suture zone, Tibetan Plateau. Geol J 55(2): 1283-1299.

Malvoisin B, Zhang C, Müntener O, Baumgartner LP, Kelemen PB, Oman Drilling Project Science Party (2020) Measurement of Volume Change and Mass Transfer During Serpentinization: Insights From the Oman Drilling Project. J Geophys Res Solid Earth 125(5), e2019JB018877.

Malvoisin B, Carlut J, Brunet F (2012) Serpentinization of oceanic peridotites: 1. A high-sensitivity method to monitor magnetite production in hydrothermal experiments. J Geophys Res Solid Earth 117(B1).

Mellini M, Rumori C, Viti C (2005) Hydrothermally reset magmatic spinels in retrograde serpentinites: formation of ‘‘ferritchromit” rims and chlorite aureoles. Contrib Miner Petrol 149: 266–275.

Merlini A, Grieco G, Diella V (2009) Ferritchromite and chromian-chlorite formation in mélange-hosted Kalkan chromitite (Southern Urals, Russia). Am Miner 94: 1459-1467.

Michailidis KM (1990) Zoned chromites with high Mn-contents in the Fe-Ni-Cr-laterite ore deposits from the Edessa area in Northern Greece. Miner Deposita 25(3): 190-197.

Moody JB (1976) An experimental study on the serpentinization of iron-bearing olivines. Can Mineral 14(4): 462-478.

Mousivand F, Rastad E, Peter JM, Maghfouri S (2018) Metallogeny of volcanogenic massive sulfide deposits of Iran. Ore Geol Rev 95: 974-1007.

Merlini A, Grieco G, Diella V (2009) Ferritchromite and chromian-chlorite formation in mélange-hosted Kalkan chromitite (Southern Urals, Russia). Am Miner 94(10): 1459-1467.

McCollom TM, Bach W (2009). Thermodynamic constraints on hydrogen generation during serpentinization of ultramafic rocks. Geochim Cosmochim Acta 73(3): 856-875.

Noghreyan M (1982) Evolution geochimique, mineralogique et structurale d'un edificeophiolitique singulier: le massif de Sabzevar (partie centrale), NE de l'Iran. TheseDoc. d'Etat, Universite de Nancy, France, p. 239.

Omrani H (2018) Island-arc and active continental margin adakites from the Sabzevar Zone, Iran. Petrology 26: 96–113. https://doi.org/10.1134/S0869591118010058

Padrón-Navarta JA, Sánchez-Vizcaíno VL, Hermann J, Connolly JAD, Garrido CJ, Gómez-Pugnaire MT, Marchesi C (2013) Tschermak's substitution in antigorite and consequences for phase relations and water liberation in high-grade serpentinites. Lithos 178: 186–196, doi:10.1016/j.lithos.2013.02.001.

Oelkers EH, Helgeson HC (1988) Calculation of the thermodynamic and transport properties of aqueous species at high pressures and temperatures: Aqueous tracer diffusion coefficients of ions to 1000 C and 5 kb. Geochim Cosmochim Acta 52(1): 63-85.

O'Neil HSC, Wall VJ (1987) The Olivine—Orthopyroxene—Spinel oxygen geobarometer, the nickel precipitation curve, and the oxygen fugacity of the Earth's Upper Mantle. J Petrol 28(6): 1169-1191.

Oufi O, Cannat M, Horen H (2002) Magnetic properties of variably serpentinized abyssal peridotites. J Geophys Res Solid Earth 107(B5), EPM-3.

Paraskevopoulos GM, Economou MI (1980) Genesis of magnetite ore occurrences by metasomatism of chromite ores in Greece. Neues Jb Miner Abh 140: 29–53.

Parkinson GS, Novotny Z, Jacobson P, Schmid M, Diebold U (2011) Room temperature water splitting at the surface of magnetite RID A-3681-2010. J Am Chem Soc 133: 12650–12655.

Prabhakar N, Bhattacharya A (2013) Origin of zoned spinel by coupled dissolution–precipitation and inter-crystalline diffusion: evidence from serpentinized wehrlite, Bangriposi, Eastern India. Contrib Miner Petrol 166(4): 1047-1066.

Putnis A, Austrheim, H (2010) Fluid-induced processes: metasomatism and metamorphism. Geofluids 10(1-2): 254-269.

Rauch EF, Véron MJMC (2014) Automated crystal orientation and phase mapping in TEM. Mater Charact 98: 1-9.

Rouméjon S, Früh-Green GL, Orcutt BN, IODP Expedition 357 Science Party (2018) Alteration heterogeneities in peridotites exhumed on the southern wall of the atlantis massif (IODP expedition 357). J Petrol 59(7): 1329-1358.

Rahmani F, Mackizadeh MA, Noghreyan M, Marchesi C, Garrido CJ (2020) Petrology and geochemistry of mafic and ultramafic cumulate rocks from the eastern part of the Sabzevar ophiolite (NE Iran): Implications for their petrogenesis and tectonic setting. Geosci Front 11(6): 347-2364

Rossetti P, Gatta GD, Diella V, Carbonin S, Della Giusta A, Ferrario A (2009) The magnetite ore districts of the southern Aosta Valley (Western Alps, Italy): a mineralogical study of metasomatized chromite ore. Mineral Mag 73: 737–751.

Shafaii Moghadam H, Corfu F, Chiaradia M, Stern RJ, Ghorbani G (2014) Sabzevar Ophiolite, NE Iran: progress from embryonic oceanic lithosphere into magmatic arc constrained by new isotopic and geochemical data. Lithos 210–211: 224–241.

Shojaat B, Hassanipak AA, Mobasher K, Ghazi AM (2003) Petrology, geochemistryand tectonics of the Sabzevar ophiolite, North Central Iran. J Asian Earth Sci 21: 1053–1067.

Spear FS (1993) Metamorphic Phase Equilibria And Pressure–Temperature–Time Paths Mineralogical Society of America,Washington, DC, 799 pp.

Sack RO, Ghiorso MS (1991) Chromian spinels as petrogenetic indicators: Thermodynamics and petrological applications. Am Miner 76(5-6): 827–847.

Santos JS, Doriguetto AC, Fernandes NG (2005) Magnesium aluminium chromite. Acta Crystallogr C 61(3): i27-i28.

Schindler M, Lussier AJ, Principe E, Mykytczuk N (2018) Dissolution mechanisms of chromitite: Understanding the release and fate of chromium in the environment. Am Miner 103(2): 271-283.

Skomurski FN, Kerisit S, Rosso KM (2010) Structure, charge distribution, and electron hopping dynamics in magnetite (Fe3O4) (100) surfaces from first principles. Geochim Cosmochim Acta 74: 4234–4248.

Sverjensky DA, Harrison B, Azzolini D (2014) Water in the deep Earth: The dielectric constant and the solubilities of quartz and corundum to 60 kb and 1200 °C. Geochim Cosmochim Acta 129: 125–145, doi:10.1016/J.GCA.2013.12.019.

Tao C, Seyfried Jr WE, Lowell RP, Liu Y, Liang J, Guo Z, Ding K, Zhang H, Liu J, Qiu L, Egorov I, Liao S, Zhao M, Zhou J, Deng X, Li H, Wang H, Cai W, Zhang G, Zhou H, Lin J, Li W (2020) Deep high-temperature hydrothermal circulation in a detachment faulting system on the ultra-slow spreading ridge. Nat Commun 11:1300. https://doi.org/10.1038/s41467-020-15062-w.

Toffolo L, Nimis P, Martin S, Tumiati S, Bach W (2017) The Cogne magnetite deposit (Western Alps, Italy): a Late Jurassic seafloor ultramafic-hosted hydrothermal system?. Ore Geol Rev 83: 103-126.

Wylie AG, Candela PA, Burke TM (1987) Compositional zoning in unusual Zn-rich chromite from the Sykesville District of Maryland and its bearing on the origin of" ferritchromit". Am Miner 72(3-4): 413-422.

Figure Captions:

Fig. 1. (a) Distribution of Mesozoic ophiolites in Iran; (b) Simplified geological map of the Sabzevar–Forumad ophiolites (modified after Shafaii Moghadam et al., 2014); (c) Simplified geological map of the study area in the eastern sector of Sabzevar ophiolite.

Fig. 2. (a) Boundins of magnetite ore-bodies hosted by highly sheared serpentinite in the Sabzevar ophiolite; (b) Sharp contact (red dashed line) between magnetite ore-body and sheared serpentinite; (c) Close-up view of aggregation of octahedral magnetite crystals embedded in pale-green serpentine.

Fig. 3. Backscattered -electron images of the Sabzevar host serpentinite (a-d) and magnetite ore (e-i). (a) partly altered chromite; (b) anhedral porous chromite; (c) close-up of porous chromite with irregular patches of Fe-chromite and associated serpentine and chlorite inclusions; (d) Skeletal andradite surrounding chromian spinel; (e) Relict of porous chromian spinel with thick magnetite rim; (f) Porous chromite associated with mylonitized magnetite; (g) Homogenous chromite with thick magnetite rim; (h) Euhedral magnetite crystals associated with andradite; (i) Individual inclusion of pentlandite in magnetite crystals from magnetite ore. Chr: chromian spinel; Mag: magnetite; Srp: serpentine; Chl: chlorite; Adr: andradite; Pn: pentlandite.

Fig. 4. Compositional plots of spinels on (a) ternary diagram Cr-Al-Fe^{3+}; (b) a X_{Cr} versus X_{Mg} diagram; (c) $Fe^{3+}/(Fe^{3+}+Fe^{2+})$ versus X_{Mg}. Reference fields of podiform chromitites in eastern sector of the Sabzevar ophiolite (Shafaii Moghadam et al., 2015; Eslami et al. 2018; unpublished data from the fisrt author) are shown for comparison.

Fig. 5. Multi-element (WDS-EDS) mapping of homogeneous chromian spinel relict in magnetite ore (sample MG15)

Fig. 6. Multi-element (WDS-EDS) mapping of a porous chromian spinel relict in magnetite ore (sample MG15)

Fig. 7. Bright Field Image (a) and EDS-STEM element maps (b to g) of the Cr-spinel / magnetite I contact. The scale bar is 500 nm. Fchr: ferritchromite. Mag I: Magnetite I.

Fig. 8. Orientation maps and selected area electron diffraction (SAED) in the reaction zone around Cr-spinel. a: orientation map in the same region as Figure 7, in which the transition from Cr-spinel to magnetite I is observed. b: supersimposed SAEDs of Cr-spinel and ferritchromite. c: superimposed SAEDs of ferritchromite and magnetite I. d: orientation map in the same region as Figure 10 at the magnetite I/magnetite II contact. e: colour-coded inverse pole figure used for displaying orientation in a and d. The boundaries between the different phases were determined with the EDS-STEM maps. CrSp: Cr-spinel; Fchr: ferritchromite. Mag I: magnetite I.

Fig. 9. High-resolution TEM images. a: contact between Cr-spinel and ferritchromite. b: contact between magnetite I and magnetite II. The red lines indicate the main orientation of the lattice planes. CrSp: Cr-spinel; Fchr: ferritchromite; Mag I: magnetite I; Mag II: magnetite II.

Fig. 10. Bright Field Image (a) and EDS-STEM element maps (b to d) of the magnetite I / magnetite II contact. The arrows indicate the location of silicate inclusions in magnetite II. The scale bar is 500 nm. Mag I : magnetite I; Mag II: magnetite II.

Fig. 11. T vs. $\Delta\log_{10}f_{O2}$ section for the Sabzevar serpentinite composition. The symbols indicate an expected evolution of $\Delta\log_{10}f_{O2}$ during cooling. They corresponds to an internally buffered oxygen fugacity (fixed by the olivine-Mg-silicate-spinel assemblage at T > 420°C and the peridotite + pure water assemblage at T < 420°C; see text for details). Stars are used as symbols when the calculation predicts the formation of a single phase. When two immiscible solid solutions are predicted to form, the composition is displayed with circles and diamonds for the Cr-rich and Fe^{3+}-rich solid solutions, respectively. The same symbols are used to display spinel composition in Fig. 12a. The red bold line separates the fields containing one (CrSp) and two (CrSp + Mt) spinels. The green bold line surrounds the chlorite stability field. Gt: garnet; Brc: brucite; Atg: antigorite; CrSp: Cr-bearing spinel; Hem: hematite; Ol: olivine; Mt: magnetite; Amp: amphibole; Cpx: clinopyroxene; Opx: orthopyroxene; Tlc: talc; Chl: chlorite.

Fig. 12. Evolution of spinel composition during cooling and oxygen fugacity decrease. The composition is displayed along a typical peridotite cooling path. The temperature and $\Delta\log_{10}f_{O2}$ conditions along this path are provided in Fig. 11 with the same symbols. a; calculated composition in the Cr-Al-Fe^{3+} ternary diagram. Stars are used as symbols when the calculation predicts the formation of a single phase. When two immiscible solid solutions are predicted to form, the composition is displayed with circles and diamonds for the Cr- rich and Fe^{3+}-rich solid solutions, respectively. b: calculated $Mg/(Mg+Fe^{2+})$ ratio

998 and brucite molar fraction along the investigated path. The Mg/(Mg+Fe^{2+}) ratios of the Cr- rich and
999 Fe^{3+}-rich spinel solid solutions are displayed with dashed and plain lines, respectively.

1000 Fig. 13. Solubilities (mol/kg) as a function of temperature along the cooling path (see text and Fig. 11
1001 for details about the path). a: Fe solubility. b: Cr solubility.

1002 Fig. 14. Schematic evolution of spinel alteration in the Sabzevar serpentinite-hosted magnetite deposit
1003 and associated peridotites

1004
1005

1006 **Table Captions:**

1007 Table S1. Representative analyses of spinels from the Sabzevar host serpentinite

1008 Table S2. Representative analyses of spinels from the Sabzevar magnetite ore. Homogeneous Cr-spinel
1009 relict (grain B) from the sample MG15 were selected for TEM

1010 Table. S3. Representative analyses of sulfides and alloys in the Sabzevar magnetite ore and host
1011 serpentinite

1012 Table S4. Representative analyses of andradite from the Sabzevar magnetite ore and host serpentinite

1013 Table S5. Representative analyses of chlorite inclusions in chromites from the Sabzevar magnetite ore
1014 and host serpentinites.

1015
1016
1017
1018
1019
1020
1021
1022
1023
1024
1025
1026
1027
1028
1029
1030

1031 Figure 1

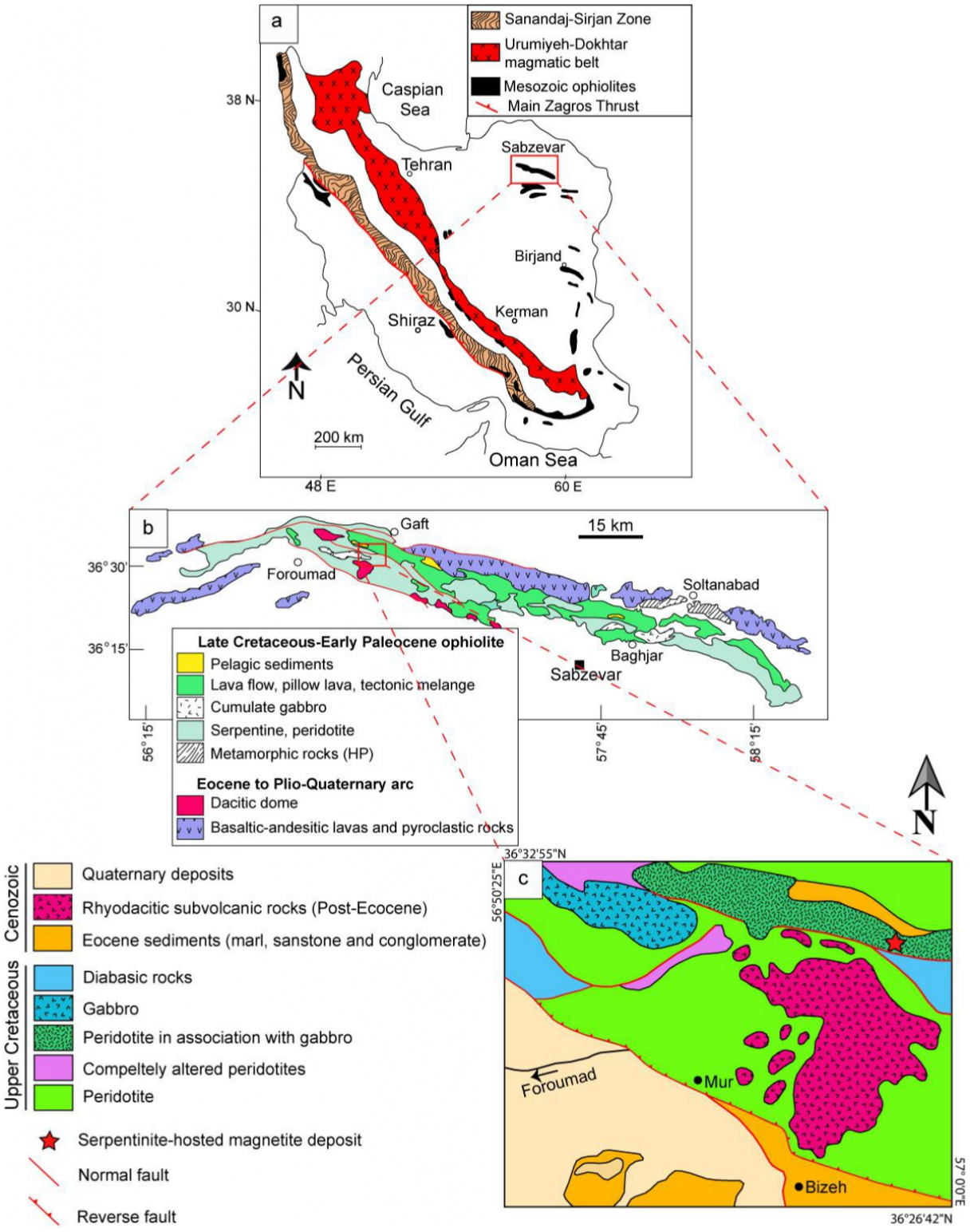

1032

1033

1034

1035

Figure 2

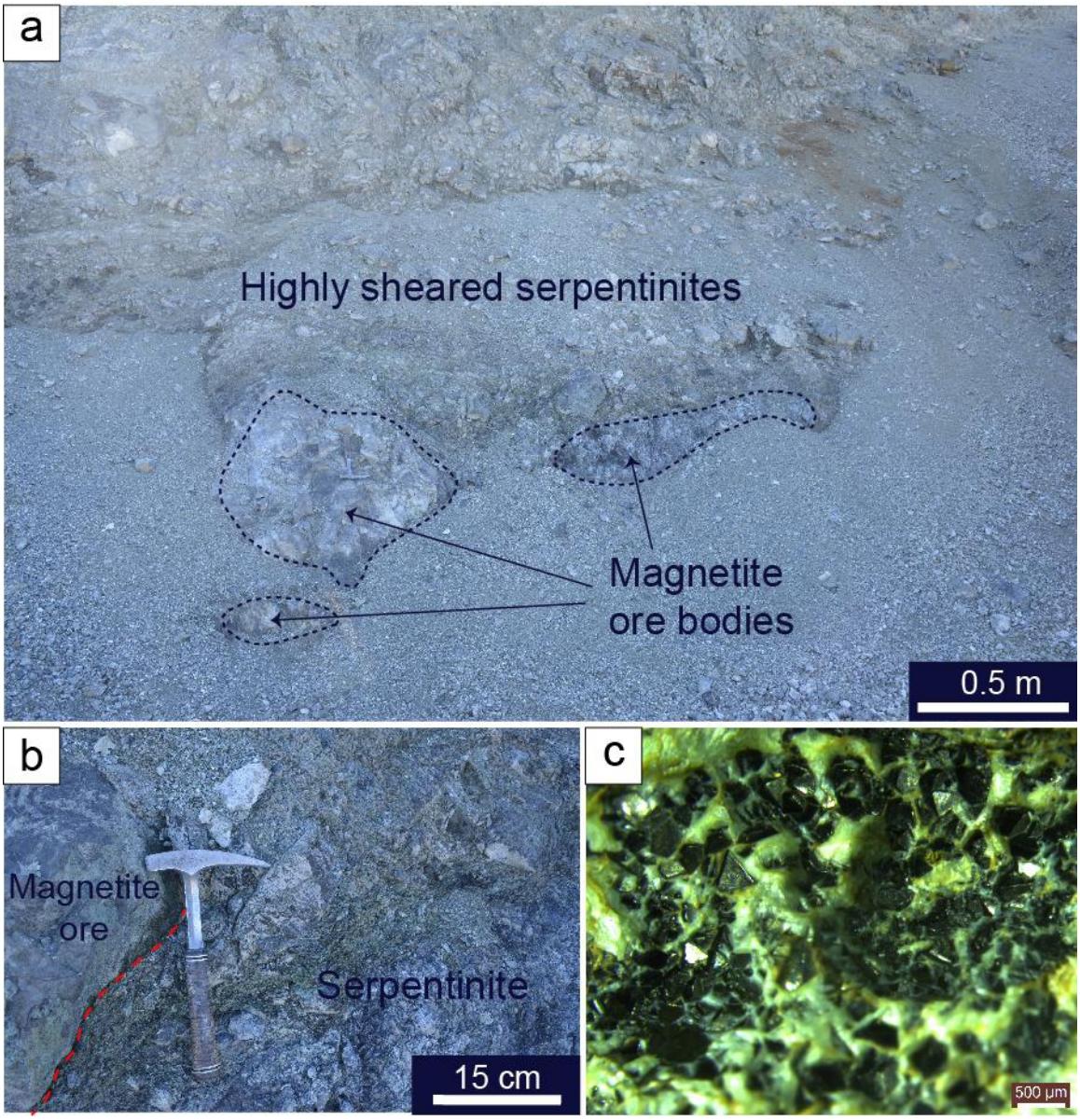
a
Highly sheared serpentinites
Magnetite
ore bodies
0.5 m
b
Magnetite
ore
Serpentinite
15 cm
c
500 µm

1044 Figure 3

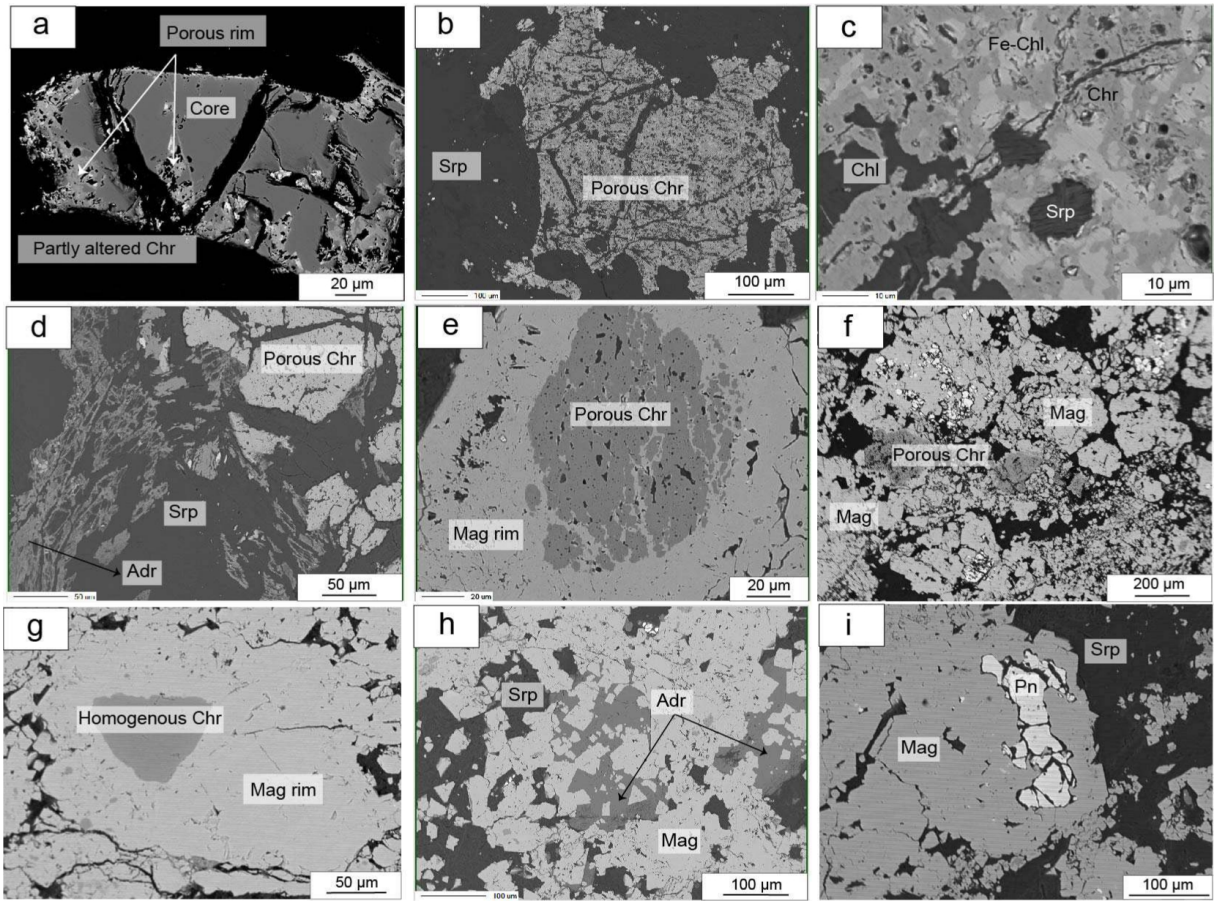

1045

1046

1047

1048

1049

1050

1051

1052

1053

1054

1055 Figure 4

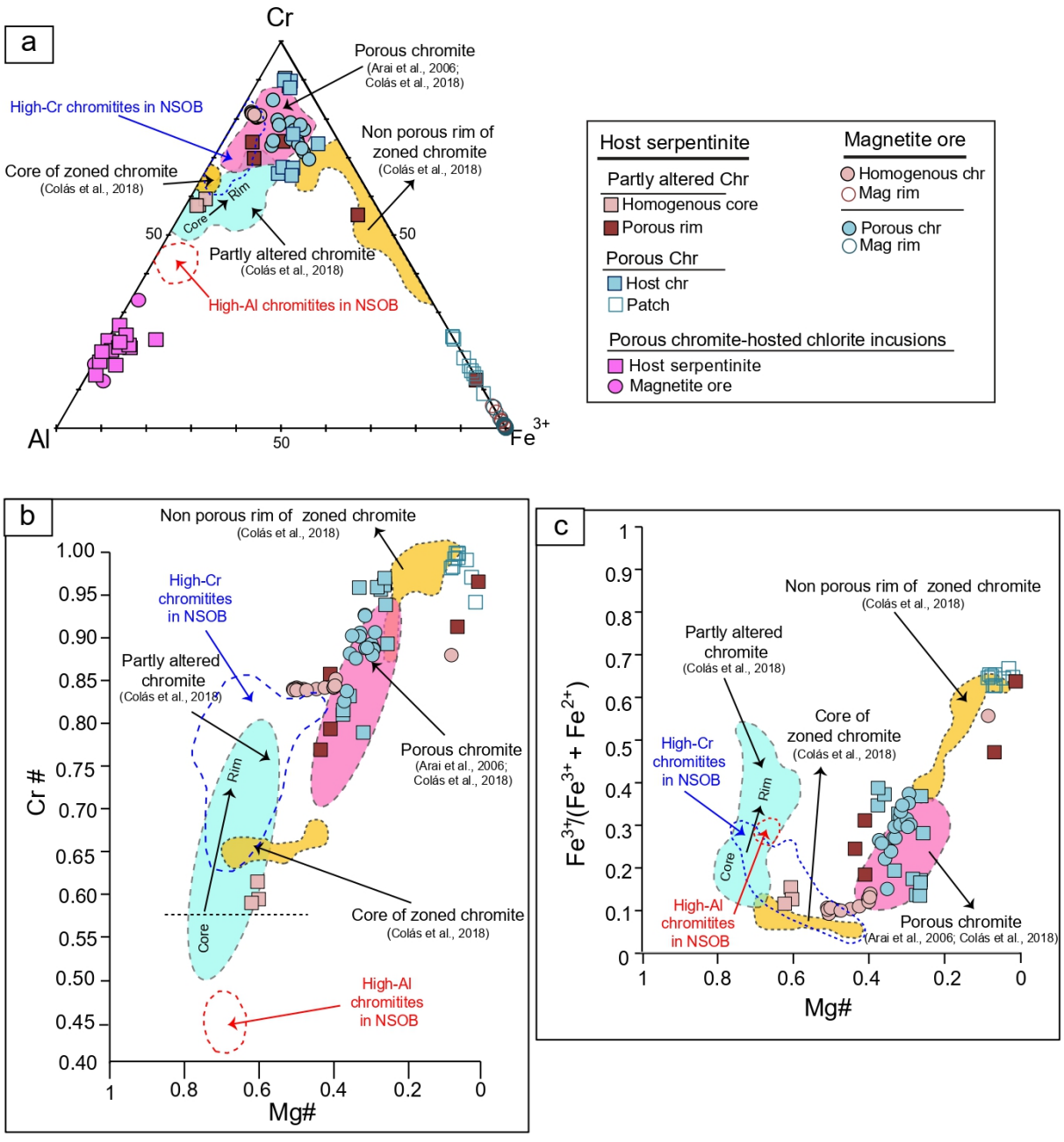

1056

1057

1058

1059

1060

1061

1062 Figure 5

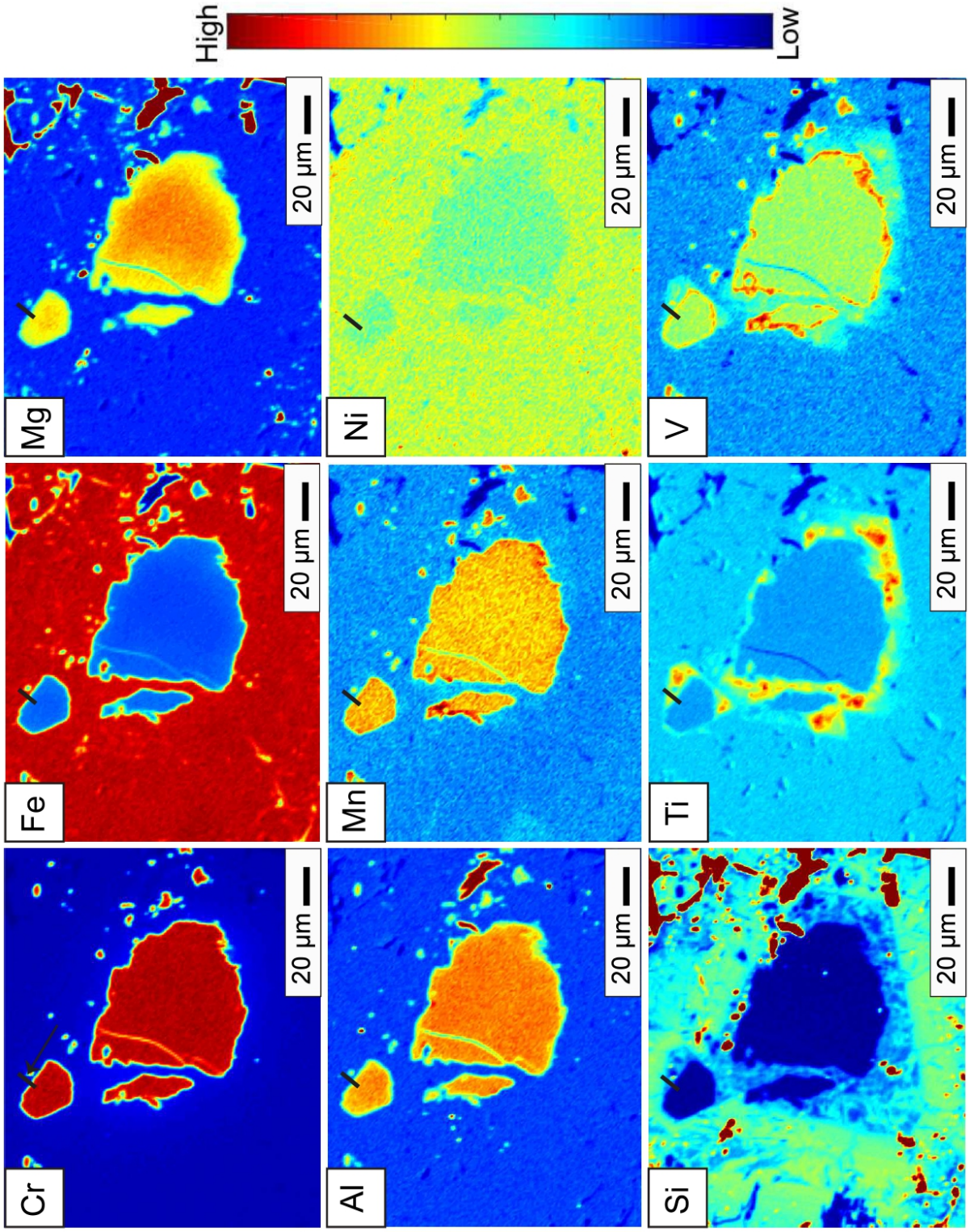

1063

Figure 6

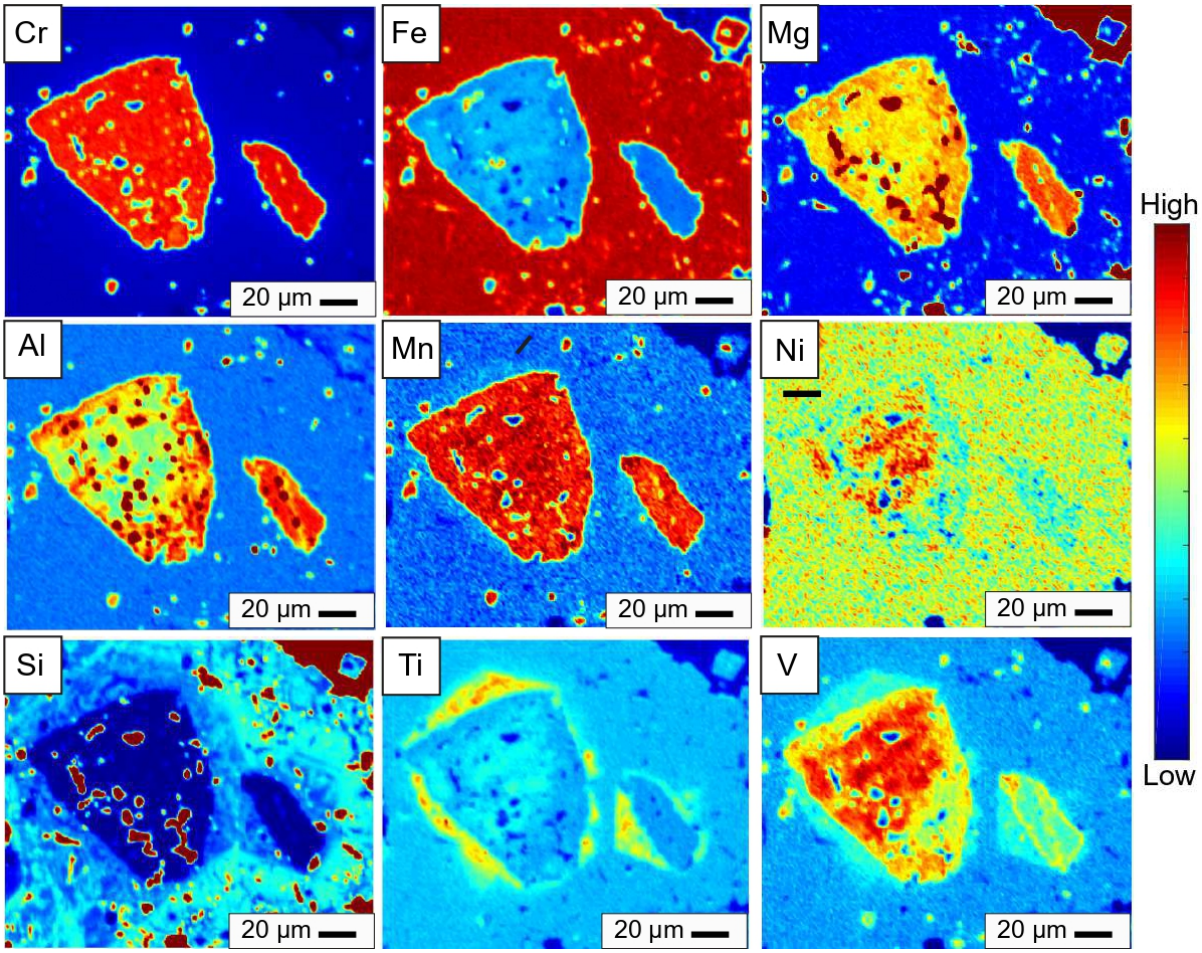

1075 Figure 7

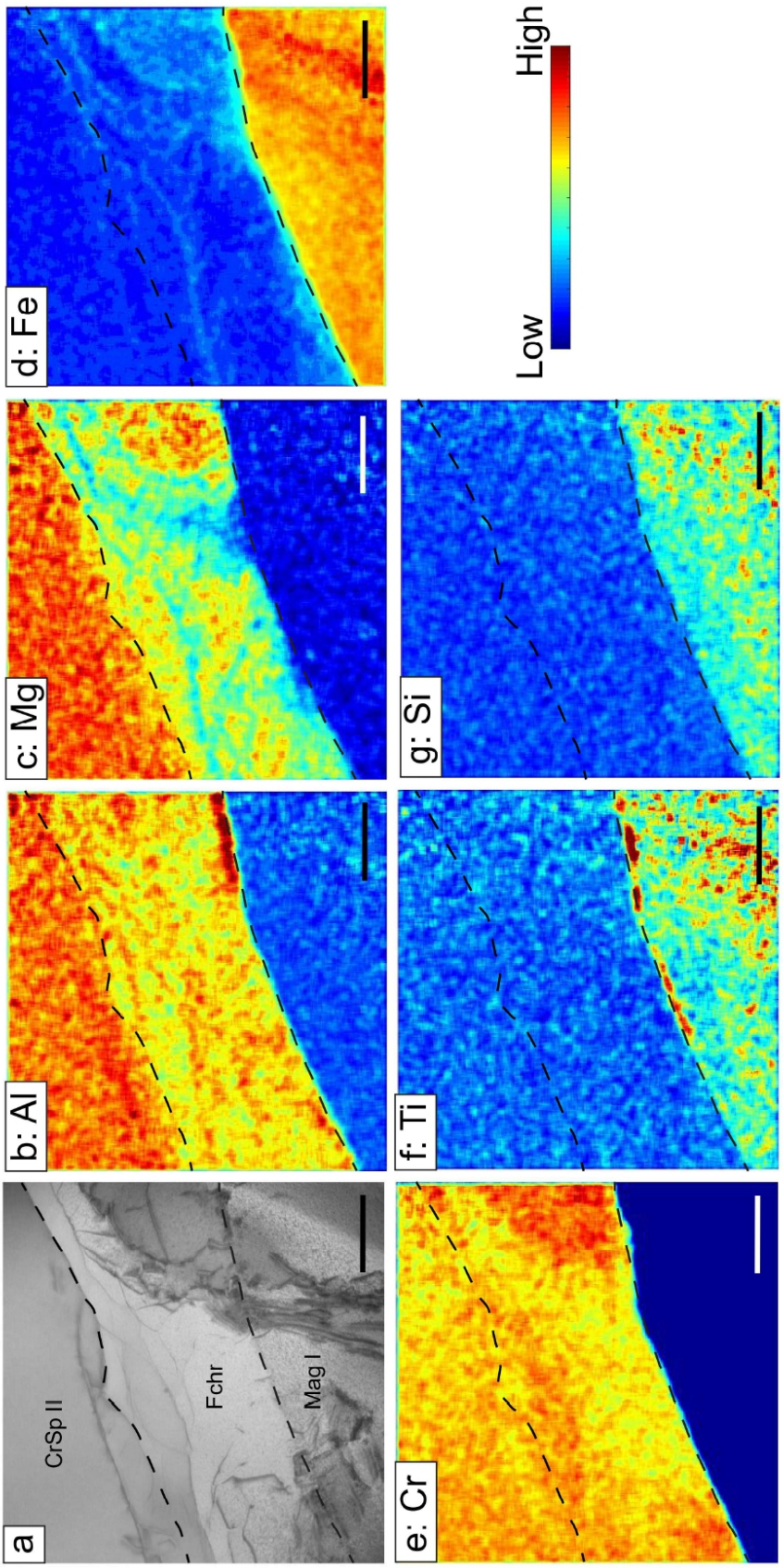

1076

1077 Figure 8

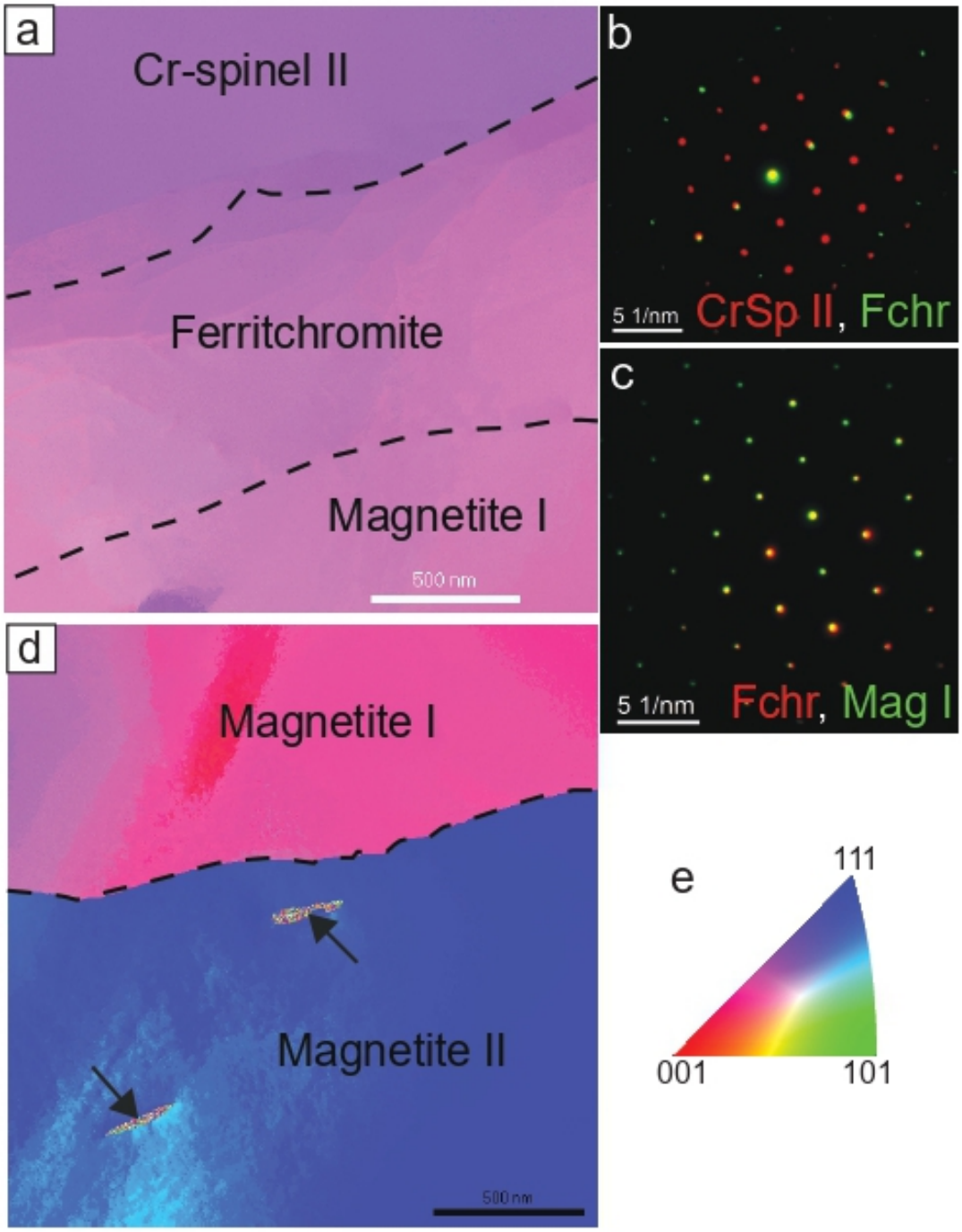

1078

1079

1080

1081

1082

1083 Figure 9

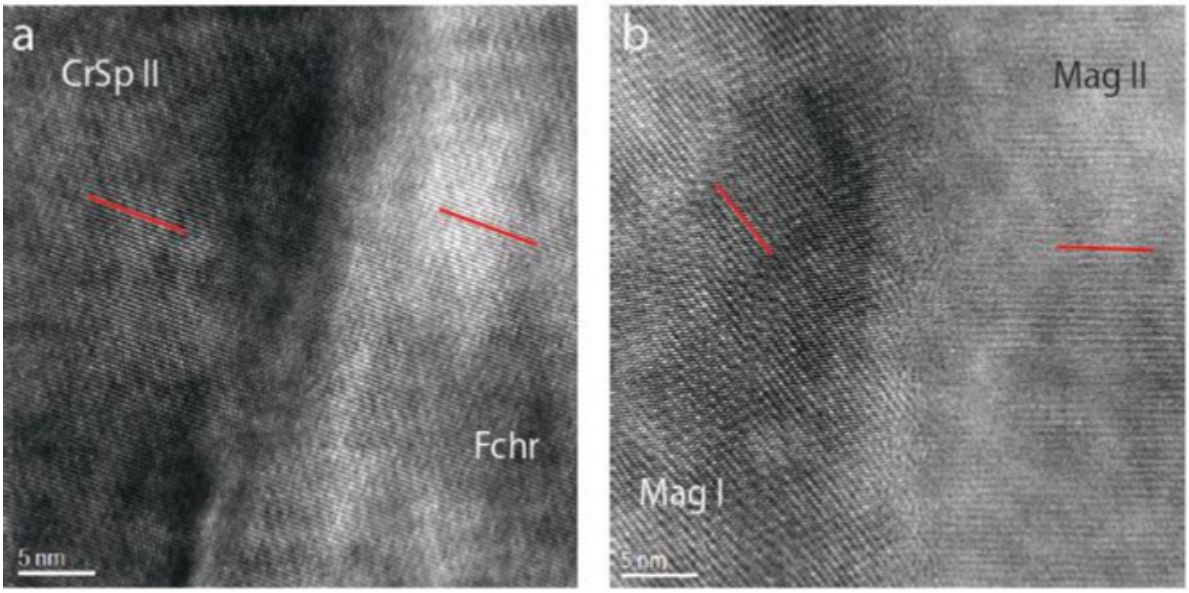

1084

1085

1086

1087

1088

1089

1090

1091

1092

1093

1094

1095

1096

1097

1098 Figure 10

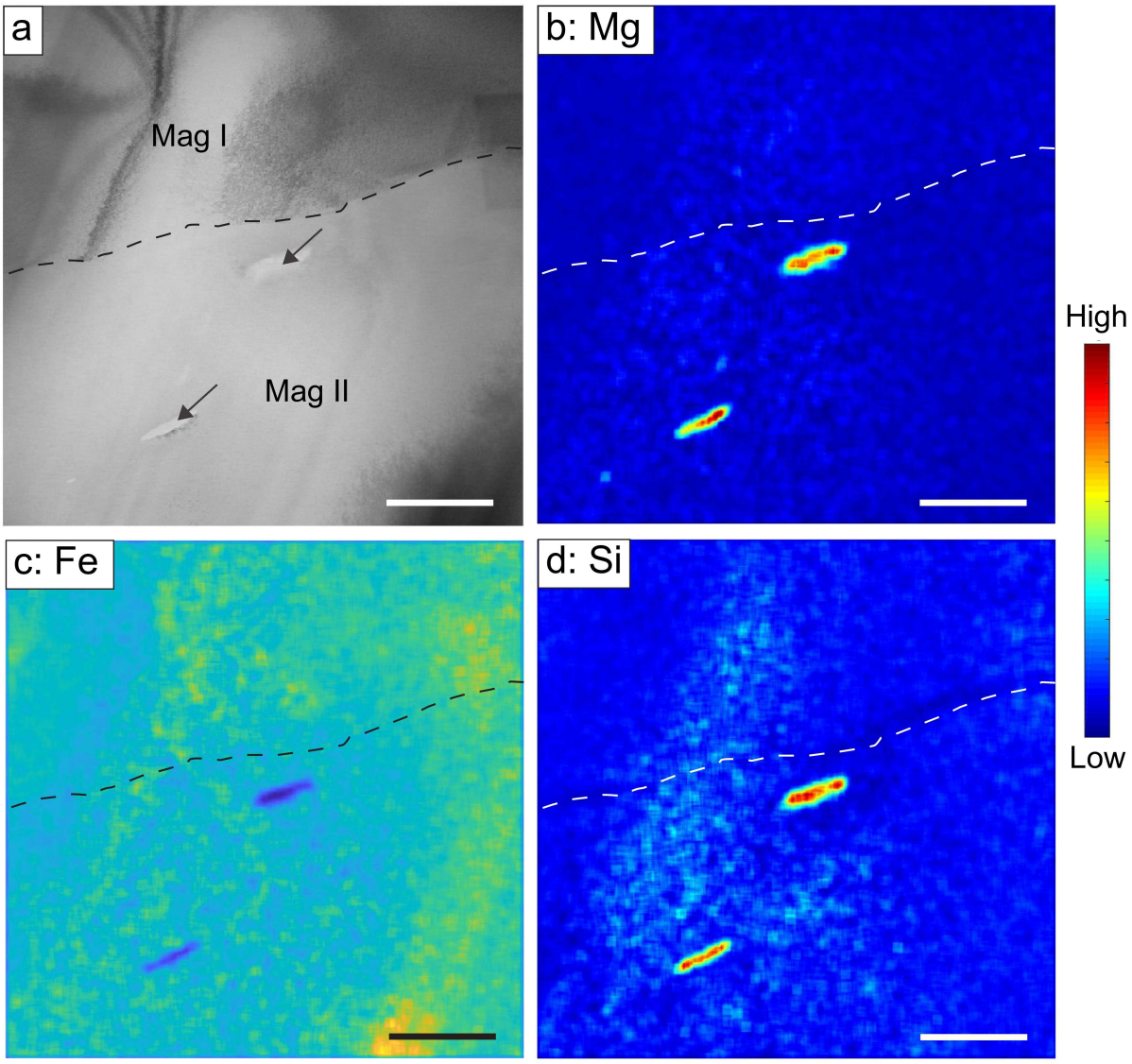

1099

1100

1101

1102

1103

1104

1105

1106

Figure 11

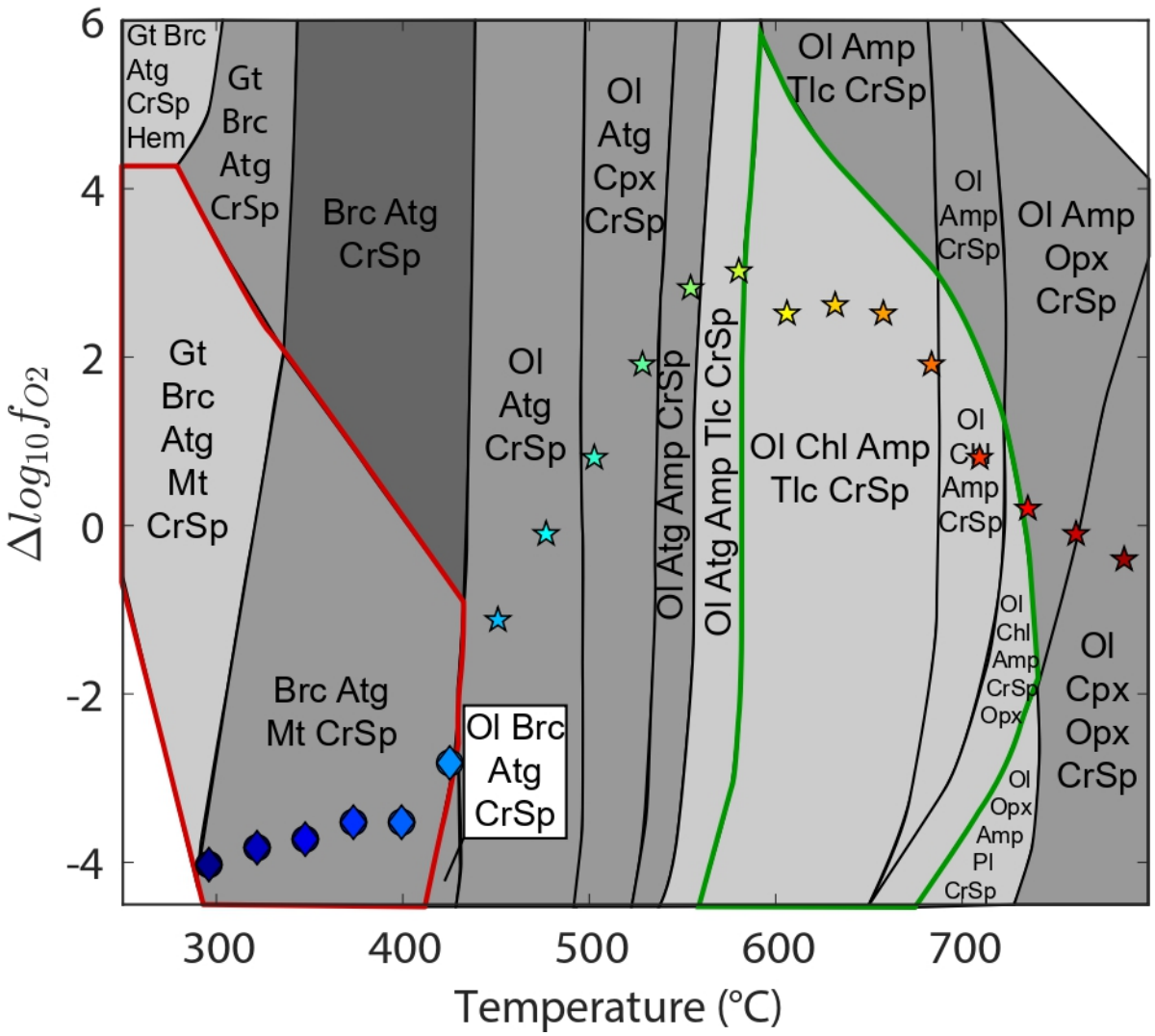
Gt Brc Atg CrSp Hem
Gt Brc Atg CrSp
Brc Atg CrSp
Ol Atg Cpx CrSp
Ol Amp Tlc CrSp
Ol Amp CrSp
Ol Amp Opx CrSp
Gt Brc Atg Mt CrSp
Ol Atg CrSp
Ol Atg Amp CrSp
Ol Atg Amp Tlc CrSp
Ol Chl Amp Tlc CrSp
Ol Chl Amp CrSp
Brc Atg Mt CrSp
Ol Brc Atg CrSp
Ol Chl Amp CrSp Opx
Ol Cpx Opx CrSp
Ol Opx Amp Pl CrSp
$\Delta log_{10} f_{O2}$
Temperature (°C)
6
4
2
0
-2
-4
300
400
500
600
700

Figure 12

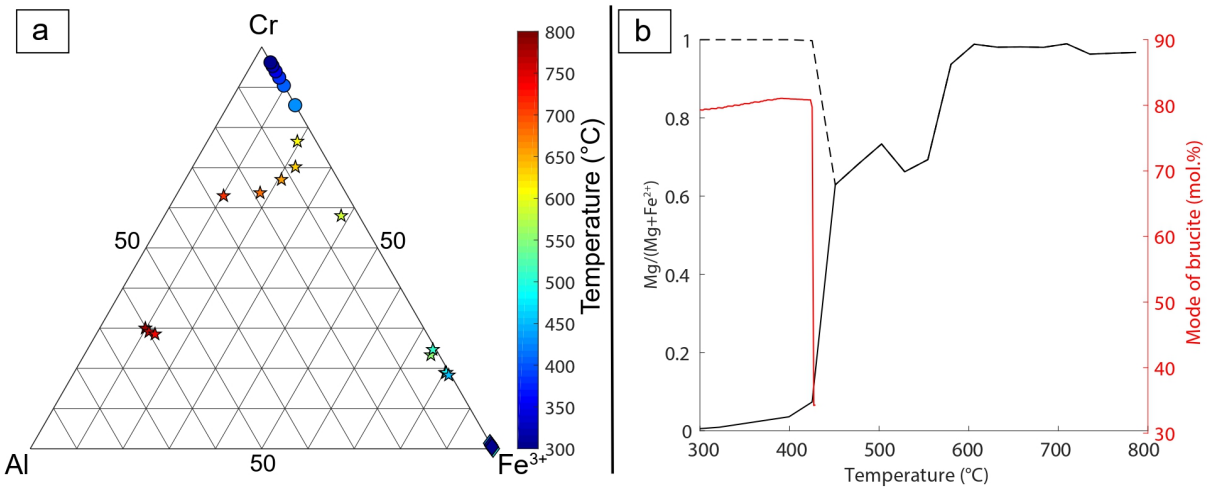
a
Cr
50
50
Al
50
Fe3+
800
750
700
650
600
550
500
450
400
350
300
Temperature (°C)
b
1
0.8
0.6
0.4
0.2
0
Mg/(Mg+Fe2+)
90
80
70
60
50
40
30
Mode of brucite (mol.%)
300
400
500
600
700
800
Temperature (°C)

1132 Figure 13

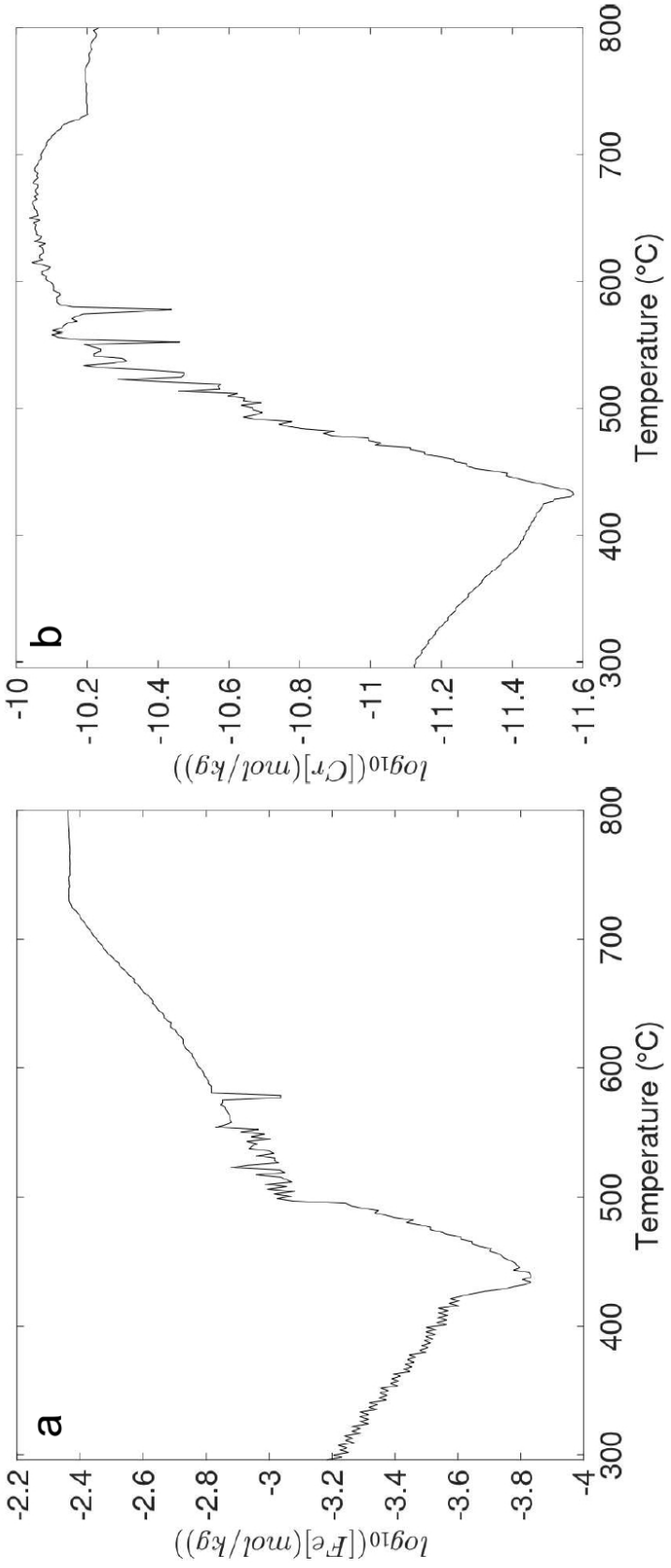

1133

1134 Figure 14

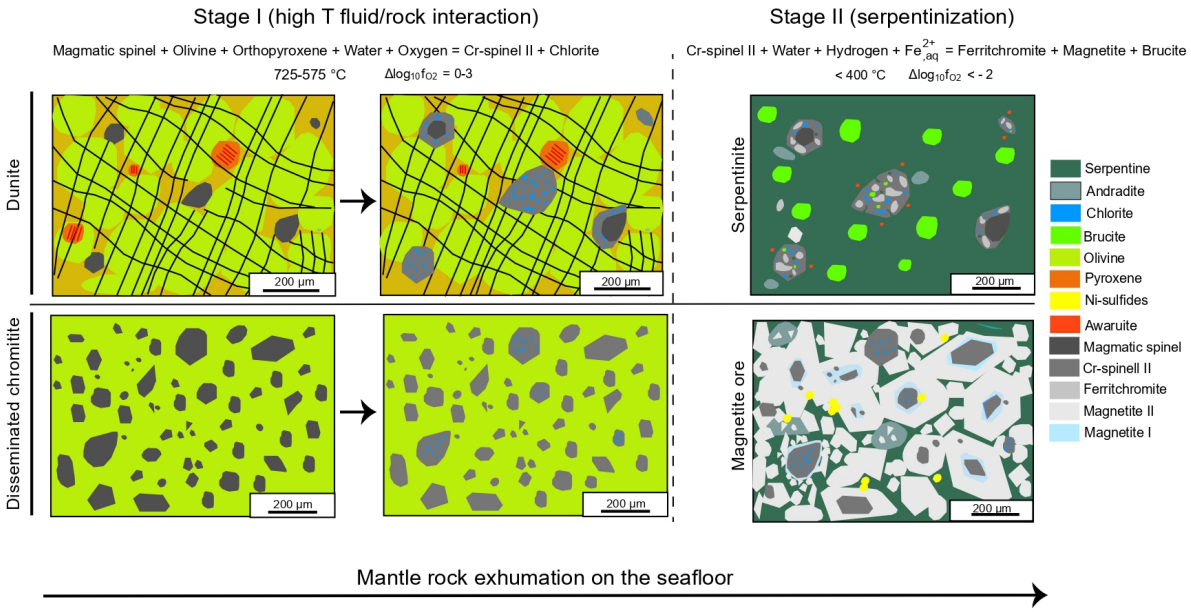

1135

1136